

Signal Response Model in PandaX-4T

Yunyang Luo,¹ Zihao Bo,² Shibo Zhang,² Abdusalam Abdukerim,² Wei Chen,² Xun Chen,^{2,3} Chen Cheng,⁴ Zhaokan Cheng,⁵ Xiangyi Cui,⁶ Yingjie Fan,⁷ Deqing Fang,⁸ Lisheng Geng,^{9,10,11} Karl Giboni,² Xuyuan Guo,¹² Chencheng Han,⁶ Ke Han,² Changda He,² Jinrong He,¹² Di Huang,² Junting Huang,² Zhou Huang,² Ruquan Hou,³ Yu Hou,¹³ Xiangdong Ji,¹⁴ Yonglin Ju,¹³ Chenxiang Li,² Jiafu Li,⁴ Mingchuan Li,¹² Shuaijie Li,^{12,2} Tao Li,⁵ Qing Lin,^{15,1,*} Jianglai Liu,^{16,2,3,†} Congcong Lu,¹³ Xiaoying Lu,^{17,18} Lingyin Luo,¹⁹ Wenbo Ma,² Yugang Ma,⁸ Yajun Mao,¹⁹ Yue Meng,^{2,3} Xuyang Ning,² Binyu Pang,^{17,18} Ningchun Qi,¹² Zhicheng Qian,² Xiangxiang Ren,^{17,18} Nasir Shaheed,^{17,18} Xiaofeng Shang,² Xiyuan Shao,²⁰ Guofang Shen,⁹ Lin Si,² Wenliang Sun,¹² Andi Tan,¹⁴ Yi Tao,^{2,3,‡} Anqing Wang,^{17,18} Meng Wang,^{17,18} QiuHong Wang,⁸ Shaobo Wang,^{2,21} Siguang Wang,¹⁹ Wei Wang,^{5,4} Xiuli Wang,¹³ Xu Wang,² Zhou Wang,^{2,3,6} Yuehuan Wei,⁵ Mengmeng Wu,⁴ Weihao Wu,² Yuan Wu,² Mengjiao Xiao,² Xiang Xiao,⁴ Binbin Yan,² Xiyu Yan,²² Yong Yang,² Chunxu Yu,²⁰ Ying Yuan,² Zhe Yuan,⁸ Youhui Yun,² Xinning Zeng,² Minzhen Zhang,² Peng Zhang,¹² Shu Zhang,⁴ Tao Zhang,² Wei Zhang,⁶ Yang Zhang,^{17,18} Yingxin Zhang,^{17,18} Yuanyuan Zhang,⁶ Li Zhao,² Jifang Zhou,¹² Ning Zhou,^{2,3} Xiaopeng Zhou,⁹ Yong Zhou,¹² Yubo Zhou,² and Zhizhen Zhou²

(PandaX Collaboration)

¹Department of Modern Physics, University of Science and Technology of China, Hefei 230026, China

²School of Physics and Astronomy, Shanghai Jiao Tong University, Key Laboratory for Particle Astrophysics and Cosmology (MoE), Shanghai Key Laboratory for Particle Physics and Cosmology, Shanghai 200240, China

³Shanghai Jiao Tong University Sichuan Research Institute, Chengdu 610213, China

⁴School of Physics, Sun Yat-Sen University, Guangzhou 510275, China

⁵Sino-French Institute of Nuclear Engineering and Technology, Sun Yat-Sen University, Zhuhai, 519082, China

⁶Tsung-Dao Lee Institute, Shanghai Jiao Tong University, Shanghai, 200240, China

⁷Department of Physics, Yantai University, Yantai 264005, China

⁸Key Laboratory of Nuclear Physics and Ion-beam Application (MOE), Institute of Modern Physics, Fudan University, Shanghai 200433, China

⁹School of Physics, Beihang University, Beijing 102206, China

¹⁰International Research Center for Nuclei and Particles in the Cosmos & Beijing Key Laboratory of Advanced Nuclear Materials and Physics, Beihang University, Beijing 100191, China

¹¹School of Physics and Microelectronics, Zhengzhou University, Zhengzhou, Henan 450001, China

¹²Yalong River Hydropower Development Company, Ltd., 288 Shuanglin Road, Chengdu 610051, China

¹³School of Mechanical Engineering, Shanghai Jiao Tong University, Shanghai 200240, China

¹⁴Department of Physics, University of Maryland, College Park, Maryland 20742, USA

¹⁵State Key Laboratory of Particle Detection and Electronics,

University of Science and Technology of China, Hefei 230026, China

¹⁶New Cornerstone Science Laboratory, Tsung-Dao Lee Institute, Shanghai Jiao Tong University, Shanghai, 200240, China

¹⁷Research Center for Particle Science and Technology, Institute of Frontier and Interdisciplinary Science, Shandong University, Qingdao 266237, Shandong, China

¹⁸Key Laboratory of Particle Physics and Particle Irradiation of Ministry of Education, Shandong University, Qingdao 266237, Shandong, China

¹⁹School of Physics, Peking University, Beijing 100871, China

²⁰School of Physics, Nankai University, Tianjin 300071, China

²¹SJTU Paris Elite Institute of Technology, Shanghai Jiao Tong University, Shanghai, 200240, China

²²School of Physics and Astronomy, Sun Yat-Sen University, Zhuhai, 519082, China

PandaX-4T experiment is a deep-underground dark matter direct search experiment that employs a dual-phase time projection chamber with a sensitive volume containing 3.7 tonne of liquid xenon. The detector of PandaX-4T is capable of simultaneously collecting the primary scintillation and ionization signals, utilizing their ratio to discriminate dark matter signals from background sources such as gamma rays and beta particles. The signal response model plays a crucial role in interpreting the data obtained by PandaX-4T. It describes the conversion from the deposited energy by dark matter interactions to the detectable signals within the detector. The signal response model is utilized in various PandaX-4T results. This work provides a comprehensive description of the procedures involved in constructing and parameter-fitting the signal response model for the energy range of approximately 1 keV to 25 keV for electronic recoils and 6 keV to 90 keV for nuclear recoils. It also covers the signal reconstruction, selection, and correction methods, which are crucial components integrated into the signal response model.

* Corresponding author: qinglin@ustc.edu.cn

† Spokesperson: jianglai.liu@sytu.edu.cn

I. INTRODUCTION

Extensive astronomical evidence, as documented in the literature [1–4], strongly indicates the ubiquitous presence of dark matter (DM) in the Universe. The nature of DM remains elusive, with various theoretical frameworks proposing that it consists either entirely or partially of unknown particles [5–7]. Among these hypotheses, the Weakly Interacting Massive Particle (WIMP) [6] stands out as one of the most promising candidates. In recent years, significant advancements in sensitivity have been achieved by DM direct search experiments conducted in deep underground laboratories [8–16]. PandaX-4T, established in May 2020, has emerged as one of the world-leading experiments of this kind. With accumulated data spanning over 92 days dedicated to WIMP search, the PandaX-4T detector has played a pivotal role in advancing our understanding in this field. Utilizing a 0.63-tonne-year exposure (Run0) conducted from November 2020 to April 2021, PandaX-4T has attained the most stringent constraint on the WIMP-nucleon spin-independent cross section at that time [14]. Subsequently, following a campaign for impurity removal in the summer of 2021, the PandaX-4T experiment resumed stable operations and has since acquired more than 164 days of additional data (Run1).

The PandaX-4T experiment utilizes a dual-phase liquid xenon (LXe) Time Projection Chamber (TPC) technique, as outlined in Ref. [14]. In this configuration, the TPC enables the detection of both prompt scintillation ($S1$) and ionized electrons generated by energy depositions. The ionized electrons undergo drift towards the top of the TPC under the influence of an applied electric field. They are subsequently extracted from the liquid phase into a thin gaseous xenon layer, where they experience a stronger amplification field. Through the process of electron luminescence, the ionized electrons are converted into secondary scintillation signals ($S2$). The $S1$ and $S2$ signals are collected by photomultiplier tubes (PMTs) positioned at the top and bottom of the TPC. Leveraging the time difference between the $S1$ and $S2$ signals, as well as the signal patterns observed on the PMTs, the longitudinal and horizontal positions (referred to as z and x - y positions) of an interaction vertex can be reconstructed. This positional information is crucial for various purposes, including distinguishing interactions originating from material or external radioactivity (e.g., those occurring near the TPC edges) and identifying interactions caused by neutrons that may exhibit multiple distinct interaction vertices within the TPC. In addition, TPCs

employing LXe as the target material possess excellent discrimination capabilities between DM-induced nuclear recoils (NRs) and background-induced electronic recoils (ERs) based on the ratio of $S2$ to $S1$. Consequently, the signal response model, which relates the deposited energy to the observable signals, plays a crucial role in interpreting DM signals within TPC-based experiments.

This paper provides a comprehensive description of the signal response model employed in the analysis of PandaX-4T results [14, 17–20]. The signal response model utilized in PandaX-4T encompasses the conversion from deposited energy to the observable signals ($S1$ and $S2$). This includes the signal production within the LXe medium, the subsequent signal collection within the TPC, and the signal reconstruction, correction, and selection during the data analysis stage. Given the inherently stochastic nature of these processes, a fast Monte Carlo (MC) simulation-based approach with the help of GPU boosting is adopted for the signal response model. This framework draws inspiration primarily from the NEST (Noble Element Simulation Technique) framework [21, 22], as well as other similar methodologies found in the literature [23]. Sec. II describes our modeling of the intrinsic signal production in LXe. The signal collection, reconstruction, correction, and selection procedures are described in Sec. III, IV, V, and VI, respectively, which are the essential detector effects in the signal response model. Furthermore, Sec. VII presents the outcomes of parameter fitting to ensure the alignment of the model with the calibration data from PandaX-4T. The obtained results from this fitting procedure are reported. Finally, a concise summary and a discussion of the findings are provided in Sec. VIII.

II. SIGNAL PRODUCTION IN LIQUID XENON

When particles interact with LXe, they transfer momentum to recoiling particles, which can be a shell electron in the case of ERs or a xenon atom in the case of NRs. These recoiling particles subsequently lose kinetic energy through elastic scattering (thermalization) and inelastic scattering (excitation and ionization) with the surrounding atoms. The total number of detectable quanta (denoted as N_q), which includes excited xenon atoms and ion-electron pairs, is directly related to the deposited energy ξ . This relationship is governed by the work function, denoted as W . The work function represents the average energy required to produce a single detectable quantum in the LXe:

$$N_q = N_i + N_{\text{ex}} = B(\xi/W, L), \quad (1)$$

where N_i and N_{ex} are the number of ion-electron pairs and excited atoms, respectively. We take a constant $W=13.7\text{eV}$ [21] in the signal response model. L is the Lindhard factor [24] characterizing the degree of heat quenching in the detection process. For ER, the Lindhard factor has a value of 1. To account for the probabilistic

† Corresponding author: taoyi92@sjtu.edu.cn

nature of the detection process, the expression $B(\xi/W, L)$ is utilized. Here, B represents a randomly sampled number generated from a binomial distribution with the number of trials being ξ/W and the success probability being L . Upon interaction with the surrounding medium, the excited xenon atom combines with a neighboring atom to form a dimer, which subsequently undergoes a decay process with a lifetime of about 4 ns or 22 ns [25]. This decay process results in the emission of a photon with a wavelength of ~ 175 nm. A fraction of the ion-electron pairs formed during the interaction can recombine and form a dimer with a surrounding atom, leading to the emission of the 175-nm ultraviolet light as well. The rest of the ionized electrons do not participate in the recombination process. The numbers of the ion-electron pairs N_i , the emitted photons N_{ph} , and the escaped electrons N_e can be written as:

$$\begin{aligned} N_i &= B\left(N_q, \frac{\alpha}{1+\alpha}\right), \\ N_e &= B(N_i, 1-r), \\ N_{\text{ph}} &= N_q - N_e, \end{aligned} \quad (2)$$

where α is the mean ratio of the numbers of the excited atoms to ion-electron pairs. The recombination fraction, denoted as r , exhibits intrinsic fluctuations based on previous discussions [26]. In the fast MC simulations, the recombination fraction is sampled from a Gaussian distribution, denoted as $G(\langle r \rangle, \Delta r)$, where $\langle r \rangle$ represents the mean fraction and Δr represents the fluctuation of recombination. The energy dependence of the mean recombination fraction, $\langle r \rangle$, is traditionally described by Birk's law [27] in the high-energy region, typically around the order of 10 keV. In the low-energy region, the energy dependence of $\langle r \rangle$ is considered to follow the Thomas-Imel model [28]. However, the existing measurements show a deviation of the $\langle r \rangle$ from the Thomas-Imel model in this low-energy region, and a global model (NEST model) [21] fitting existing data is usually used in the community. The availability of measurements for the mean recombination fraction ($\langle r \rangle$) and its fluctuation (Δr) is limited in this low-energy region due to the difficulty of getting keV and sub-keV energy depositions in a dense detector. Consequently, the nominal values provided by NESTv2 [22] have uncertainties associated with them. In the PandaX-4T experiment, we have performed further tuning of the model parameters using our own calibration data to refine the values of $\langle r \rangle$ and Δr . The details of this tuning will be presented in Sec. VII.

III. SIGNAL COLLECTION

TPC detects the primary scintillation $S1$ signals and the secondary scintillation $S2$ signals with different features.

The prompt scintillation signals, $S1$, are collected

shortly after the particle interaction, typically within a time scale of 10 to 100 ns. However, the collection of $S1$ signals is associated with a success probability, typically around 0.1 to 0.2 in dual phase TPCs. This success probability, also known as the photon detection efficiency (PDE), is spatially dependent and influenced by various factors. These factors include the coverage of PMTs within TPC, as well as the collection efficiency and quantum efficiency of the PMTs themselves. The PDE is also affected by the purity level of the LXe, which can influence the absorption length of scintillation photons, and the reflection properties of the Polytetrafluoroethylene (PTFE) reflectors used in the TPC. The number of collected photons N_{det} is related to the number of photons generated N_{ph} and can be written as:

$$N_{\text{det}} = B(N_{\text{ph}}, \varepsilon_{\text{PDE}}(x, y, z)), \quad (3)$$

where ε_{PDE} represents the spatially dependent PDE.

When a photon is detected by a PMT and converted into a photoelectron (PE) inside the PMT, there is a phenomenon known as double PE emission (DPE). This phenomenon refers to the emission of multiple photoelectrons from the PMT photocathode as a result of the initial detection of a single photon. In the case of 175-nm ultraviolet (UV) light, it has been observed that there is an approximately 20% probability for a single detected photon to generate two photoelectrons within the PMT [29]. The number of the PEs N_{pe} that are generated inside PMTs can be expressed as:

$$N_{\text{pe}} = N'_{\text{det}} + B(N'_{\text{det}}, p_{\text{dpe}}), \quad (4)$$

where p_{dpe} represents the probability of DPE. We usually take $g_1 = \langle \varepsilon_{\text{PDE}} \rangle \cdot (1 + p_{\text{dpe}})$ as a characteristic parameter for $S1$ detection. $\langle \varepsilon_{\text{PDE}} \rangle$ is the average PDE inside the fiducial volume (FV). The spatial dependence of $\varepsilon_{\text{PDE}}(x, y, z)$ is obtained using calibration data, which will be illustrated in Section V. Note that the N'_{det} in Eq. 4 represents the number of photons that are successfully clustered during signal reconstruction, which will be detailed in Section IV.

The $S2$ signal in the PandaX-4T detector is obtained by the detection of secondary scintillation light emitted when the ionized electrons undergo drift in the sensitive volume and reach the gaseous xenon region. During the drifting process, electron attachment can occur, when some of the drifting electrons become bound to electro-negative impurity molecules present in the LXe. The probability of electron attachment is dependent on factors such as the concentration and type of impurity. In the PandaX-4T detector, the most prevalent and dominant electro-negative impurity is oxygen. The number of electrons that survive the drifting process and reach the gaseous xenon layer, denoted as N_{drift} , can be written in the form:

$$N_{\text{drift}} = B(N_e, e^{-z/(\tau_e v_{\text{drift}})}), \quad (5)$$

where v_{drift} is the constant drift velocity of the electrons in LXe, and τ_e is the electron lifetime which is an indicator of the impurity level. Throughout Run0 and Run1 of the PandaX-4T, the operation of the TPC was subject to various procedures and incidents, such as power outages. These events led to the introduction of impurities into the TPC, despite the continuous circulation and purification of the LXe. The evolution of the electron lifetime was monitored during this period using residual α events originating from ^{222}Rn decays (as shown in Fig. 1), as well as X-ray events resulting from the decays of neutron-activated $^{129\text{m}}\text{Xe}$ and $^{131\text{m}}\text{Xe}$.

The drifted electrons are subsequently extracted into the gaseous xenon layer of the TPC. However, it is worth noting that if the extraction electric field strength is insufficient, a fraction of the electrons may fail to be extracted, leading to a signal loss. The number of extracted electrons N_{ext} can be written as:

$$N_{\text{ext}} = B(N_{\text{drift}}, \varepsilon_{\text{ext}}), \quad (6)$$

where ε_{ext} represents the extraction efficiency. Once extracted, the electrons pass through the gaseous xenon medium, inducing excitation in the surrounding xenon atoms, which subsequently emit 175-nm ultraviolet (UV) light. These light signals are collected and converted into PEs by the PMTs. The number of PEs of these light signals N_{prop} then is modelled as

$$N_{\text{prop}} = G\left(\kappa(x, y)N_{\text{drift}}, \Delta\kappa\sqrt{N_{\text{drift}}}\right). \quad (7)$$

The overall amplification gain, denoted as κ , is determined by the combined factors of light collection efficiency, the gas gap thickness, and the strength of the amplification field. However, the amplification process is subject to non-uniformities in the amplification field, leading to fluctuations in the total gain. These fluctuations are quantified by the parameter $\Delta\kappa$, which typically exhibits magnitudes on the order of 20% to 40% of κ . To describe the amplification of the charge signal, a commonly employed parameter is defined as $g_2 = \langle\kappa\rangle\varepsilon_{\text{ext}}$ where $\langle\kappa\rangle$ is the average of κ within the FV. The spatial dependence of $\kappa(x, y)$ is illustrated and given in Sec. V. In order to have time-independent charge amplification in the data, the temporal feature of κ is corrected (discussed in later Sec. V) and shown in Fig. 2. Note that in the PandaX-4T analysis, the $S2$ signals from bottom PMTs are used. The $S2$ distribution on the bottom PMTs is more spread than the one on the top PMTs, reducing the chance of PMT saturation for $S2$ s. Therefore, we use the corresponding parameter $g_{2\text{b}} = \langle\kappa_{\text{b}}\rangle\varepsilon_{\text{ext}}$ as the parameter for describing the $S2$ gain.

Both g_1 and $g_{2\text{b}}$ can be determined by analyzing calibration data. Following the charge correction steps discussed later in Sec. V, g_1 and $g_{2\text{b}}$ are fitted by ER peaks of $^{83\text{m}}\text{Kr}$ (41.5 keV), $^{131\text{m}}\text{Xe}$ (163.9 keV) and $^{129\text{m}}\text{Xe}$ (236.2 keV), according to the energy

reconstruction formula:

$$\xi = W\left(\frac{Q_{S1}^c}{g_1} + \frac{Q_{S2\text{b}}^c}{g_{2\text{b}}}\right) \quad (8)$$

where Q_{S1}^c and $Q_{S2\text{b}}^c$ are the corrected $S1$ and $S2$ charges, respectively. The lower b indicates the $S2$ charge is obtained from only the bottom PMTs. The correction here refers to the correction for signal's spatial non-uniformity, which will be detailed in Subsection V A. In order to establish a unified signal response model for the entire data-taking period of PandaX-4T, the parameters (g_1 , $g_{2\text{b}}$) for Run0 and Run1 data are considered to differ by a factor due to variations in operating conditions, specifically electric fields and liquid levels. Using the α events from ^{222}Rn decay, we obtain that the g_1 in Run1 is 9% smaller than that in Run0, and $g_{2\text{b}}$ 22% larger. Next, the corrected $S1$ and $S2_{\text{b}}$ yields, defined as the number of detected PEs (corrected) in the $S1$ and $S2_{\text{b}}$ signals per unit of energy, are measured for six ER peaks originating from $^{83\text{m}}\text{Kr}$ (41.5 keV), $^{131\text{m}}\text{Xe}$ (163.9 keV), and $^{129\text{m}}\text{Xe}$ (236.2 keV) in both Run0 and Run1 data sets. The distributions of corrected $S1$ and $S2_{\text{b}}$ yields, often referred to as Doke plots, in Run0 and Run1 are simultaneously fitted to obtain the g_1 and $g_{2\text{b}}$. Fig. 3 illustrates the distributions of corrected $S1$ and $S2_{\text{b}}$ yields from the six ER peaks, and the best fit of g_1 and $g_{2\text{b}}$.

IV. SIGNAL RECONSTRUCTION

The impact of signal reconstruction on the signal response model is substantial due to several factors. The region of interest (ROI) that we focus on is characterized by low deposit energy, making it susceptible to various sources of fluctuations introduced during the trigger, reconstruction, and correction processes. Additionally, the presence of noise, PMT afterpulsing, photoionization effects, and delayed electrons complicates the data selection process. These factors collectively contribute to the considerable influence of signal reconstruction on our model's accuracy. In this section, we provide a detailed description of the sequential steps involved in signal reconstruction and present an effective model for signal reconstruction within the signal response model.

A. Hit finding and clustering

Following the collection and amplification of the 175-nm light signal by the PMTs, the resulting signal is passed to the V1725 fast analog-to-digital converter (FADC). To reduce data size, we employ the Zero Length Encoding (ZLE) mode within the FADC. This mode involves setting a ZLE threshold, which is determined as approximately one-third of the single PE amplitude (20 ADC units). Only waveform segments that exceed this threshold are recorded. For each

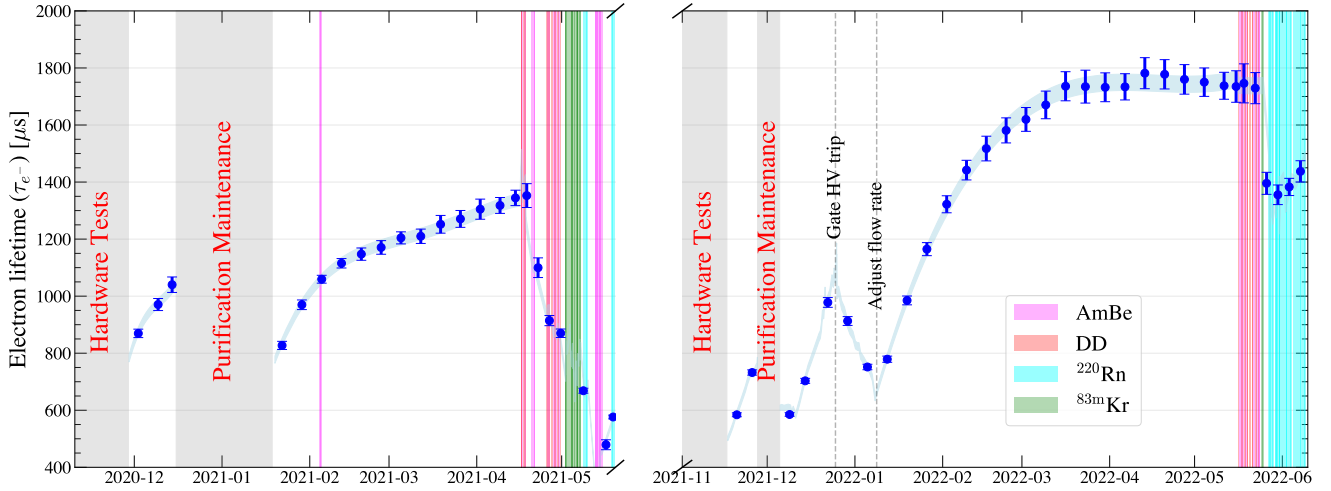


FIG. 1. The electron lifetime evolutions in Run0 and Run1 scientific data taking periods. The gray shaded regions indicate the time periods for detector operations. The period of calibration runs are present as well, including $^{241}\text{AmBe}$ (magenta), DD (red), ^{220}Rn (cyan), and $^{83\text{m}}\text{Kr}$ (green).

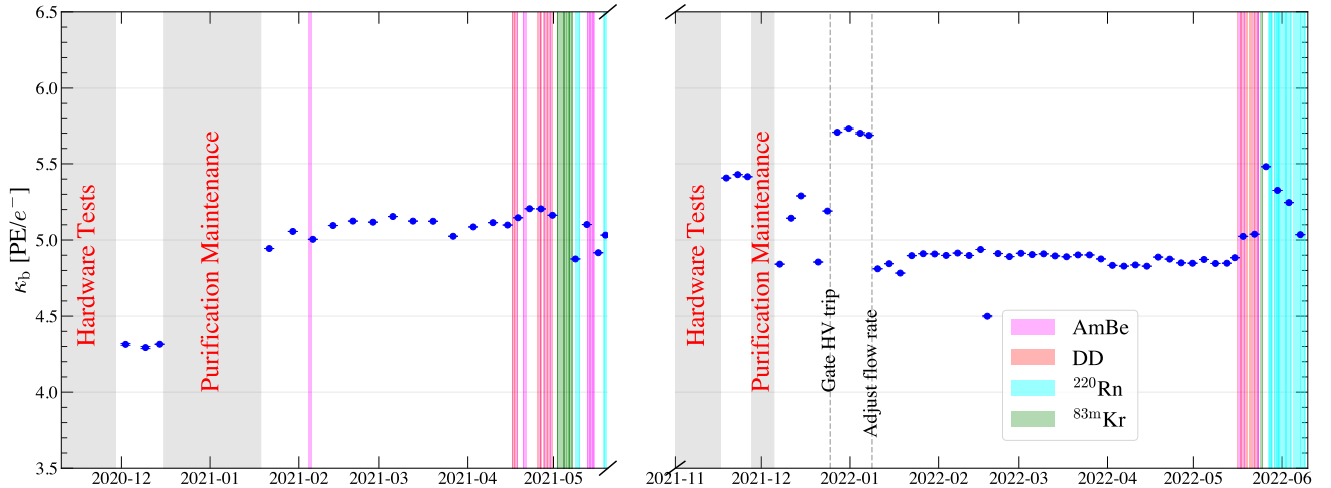


FIG. 2. The evolution of κ in Run0 and Run1 data taking periods. The gray shaded regions indicate the time periods for detector operations. The period of calibration runs are present as well, including $^{241}\text{AmBe}$ (magenta), DD (red), ^{220}Rn (cyan), and $^{83\text{m}}\text{Kr}$ (green).

PMT channel, waveform segments are first subtracted by their respective baselines, which are calculated segment-by-segment. The single hit is then constructed once the amplitude exceeds the 2.44 mV (20 ADC) threshold and continues until there are 80 ns of continuous sampling points whose amplitudes are below this threshold. To keep enough duration for baseline calculation, the shortest duration of one segment is set to be 400 ns. These single hits serve as the fundamental units within the entire data structure throughout the

PandaX-4T data analysis process. Based on these single hits, we further define the concepts of signal and physical event. The single hits across the PMT channels are further clustered into a single pulse, once the time difference of any two adjacent hits in the clustered pulse is less than 60 ns.

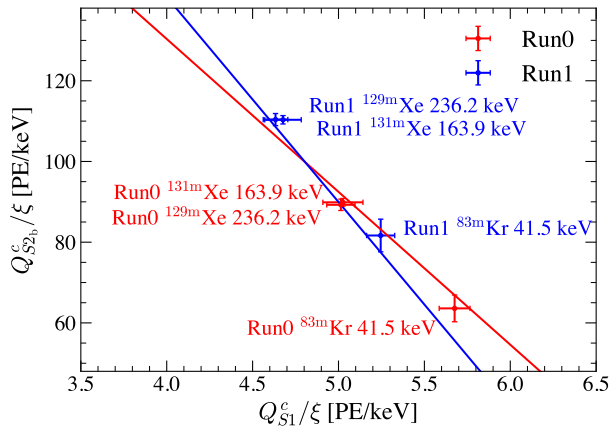


FIG. 3. The corrected $S1$ and $S2_b$ yields obtained from ^{83m}Kr , ^{131m}Xe , and ^{129m}Xe in Run0 (red) and Run1 (blue) data. A Run0-Run1 combined fit is performed using these corrected $S1$ and $S2_b$ yields to obtain the g_1 and g_{2b} , with a projection line being plotted for both runs. The best fit (g_1 , g_{2b}) values for Run0 and Run1 are $(0.103 \pm 0.005, 3.9 \pm 0.4)$ and $(0.093 \pm 0.004, 4.7 \pm 0.5)$, respectively.

B. Pulse classification

The clustered pulses are further categorized into $S1$ and $S2$ pulses based on their different characteristics. $S1$ lights are generated almost instantly after the incident particle collides with the target nucleus, resulting in a narrow pulse. Additionally, the $S1$ lights are generated in the LXe region below the liquid-gas surface. Due to the total internal reflection effect at the liquid-gas interface, the $S1$ signal received by the bottom PMTs is greater than that received by the top. On the contrary, the generation of $S2$ signals involves the electron drifting which is affected by diffusion, and the continuous acceleration and extraction of electrons in the gaseous layer under a stronger electric field, resulting in a larger amplitude and a more spread time profile of the $S2$ lights. Since the $S2$ lights are generated in gaseous xenon and closer to the top PMTs, the top PMTs receive more lights.

With these considerations, the classification of $S1$ and $S2$ pulses is primarily based on the pulse shape and its distribution across the PMTs. To characterize the charge partition between the top and bottom PMT arrays, we define the Top-Bottom Asymmetry (TBA) as $\text{TBA} = (q_t - q_b)/(q_t + q_b)$, where $q_{t/b}$ represents the accumulated charge of the pulse from the top/bottom PMTs. Additionally, the full width of the pulse is defined as the difference of the reconstructed left and right boundaries (over-threshold times with some buffer) of the pulse, which is affected by the afterglow effect. To better characterize the pulse duration while mitigating the afterglow effect following the major pulses, we also introduce a pulse width metric called CDF width.

This width is determined by the time interval that encompasses the cumulative charge from 10% to 90% of the pulse and is denoted as w_{CDF}^{90-10} . In the data processing of PandaX-4T, the analysis program iterates over all clustered pulses and assigns different types to each pulse. The classification discussed in this work primarily focuses on the low-energy region (< 25 keV for ER or < 90 keV for NR). Before the classification, noise and discharging pulses are pre-identified based on their abnormal waveform shapes and concentrated distributions. Signals larger than 10^6 PE with narrow widths and negative TBA values, or signals larger than 10^4 PE with one PMT channel accounts for more than 40% of the total signal charge, are determined to be due to discharging. Subsequently, the $S1$ and $S2$ pulses are identified with relatively loose filtering conditions compared to the final data selection. For $S2$ pulses, a minimum total charge of 15 PE is required, along with triggering of at least five PMTs and a TBA above a charge-dependent lower limit. Furthermore, the full width of $S2$ pulses must be larger than 320 ns, and w_{CDF}^{90-10} must exceed 240 ns. Regarding $S1$ pulses, the total charge is accepted down to 0.3 PE (corresponding to the ADC threshold of a single hit), with a charge-dependent upper limit for TBA. Low-energy $S1$ pulses are also required to have w_{CDF}^{90-10} less than 320 ns.

C. $S1$ - $S2$ Pairing

In a TPC detector, a typical physical event is characterized by the presence of one $S1$ pulse accompanied by at least one associated $S2$ pulse. In the case of multiple scatters (MSs), multiple $S2$ pulses are present. To define the time window for a physical event, we primarily consider a window extending 1 ms before and after the start time of the first arrived $S2$ pulse, which serves as the anchor $S2$. The anchor $S2$ is subject to updating if a subsequent $S2$ pulse with three times larger total charge is found within the event window. In this case, the window's right boundary is extended to 1 ms after the updated anchor $S2$, and the left boundary is synchronously redefined as 1 ms before it. This updating procedure is iterated until no more update on the anchor $S2$ is needed. The 1-ms window is chosen so that it is sufficiently larger than the maximum drift time of the TPC, which are approximately 840 and 850 μs in Run0 and Run1, respectively.

Once the event window is determined, the major $S2$ pulse is identified as the pulse with the largest total charge. This pulse is considered to be the primary $S2$ signal associated with the event. To enhance the pairing efficiency between $S1$ and $S2$ signals in physical events, several selection criteria are applied to the major $S1$ signal. These criteria aim to distinguish it from single electron (SE) fragments that may be incorrectly tagged as $S1$ pulses. The major $S1$ pulse is required to be “clean”, meaning that no other signals should appear in

its temporal vicinity (within 400 ns before and after). Additionally, the major $S1$ pulse should not have more than 5 peaks [30], and its w_{CDF}^{90-10} is constrained to a maximum of 240 ns. Furthermore, to distinguish the major $S1$ pulse from pulses due to discharging, it is required that the light distribution of the major $S1$ pulse is not excessively concentrated on the top and bottom PMT arrays. We use the area of a single hit (A_{hit}) in the waveform to quantify the concentration of the light signal, and set upper limits to the largest hit area detected from top and bottom PMT arrays, respectively. Since the TBA distribution of $S1$ (TBA_{S1}) has been tested to be consistent between waveform simulation and calibration data [31]. The 99.5% quantile derived from waveform simulation in the parameter space of $\text{TBA}_{S1} - M(\text{TBA}_{S1})$ as a function of Q_{S1} is applied as an upper bound, where $M(\text{TBA}_{S1})$ denotes the median values with respect to the drift time dt , as shown in Fig. 4. The largest of the $S1$ pulses that satisfy the criteria within the physical event window before the first arrived $S2$ is determined as the major $S1$.

D. $S2$ reclustering

In the analysis of PandaX-4T data, an additional reclustering procedure is applied to the largest and second-largest $S2$ s in a physical event. This step is necessary to address the problem of the initial clustering method, which combines two adjacent hits into one cluster if they are less than 60 ns apart in time. It has been observed that this approach can lead to incorrect fragmentation of hits that actually belong to an $S2$ signal. To overcome this issue, the reclustering algorithm utilizes the $S2$ width relation with the $S2$ vertical position due to electron diffusion. For each instance of the largest and second-largest $S2$ waveform, the clustering width is redefined and adjusted based on factors such as the vertical position and the $S2$ size.

In the reclustering process of PandaX-4T, the determination of whether to merge each nearest neighbor pulse into a major $S2$ signal is performed based on whether the inclusion would result in a $S2$ w_{CDF}^{90-10} that complies with the expected $S2$ width due to diffusion. Based on the distribution of the $S2$ w_{CDF}^{90-10} as a function of drift time t , the standard deviation $\sigma_{\text{ori}}(t)$ of the $S2$ w_{CDF}^{90-10} as a function of drift time is derived. The nearby small signal is merged if its resulted w_{CDF}^{90-10} increment is less than $1.5\sigma_{\text{ori}}(t)$. For $S2$ signals smaller or larger than 1000 PE, the reclustering is forced to stop when the merged $S2$ signal's w_{CDF}^{90-10} deviates by 5σ or 3σ , respectively, from the expected w_{CDF}^{90-10} of the initial $S2$ before the reclustering. Additionally, the horizontal distance between signals (< 200 mm for $Q_{\text{signal}} > 10$ PE) is taken into account to ensure spatial proximity, suggesting a common origin for the merging candidates.

E. Position reconstruction

The vertical position in the PandaX-4T experiment is determined by multiplying the drift velocity by the time difference between the $S1$ and $S2$ signals. For horizontal position reconstruction in the PandaX-4T experiment, two algorithms have been developed: the template matching (TM) and the photon acceptance function (PAF) methods. These algorithms are designed to determine the scattering position of each event based on the signals collected by the top PMT array during the $S2$ signal. More details of the position reconstruction can be found in Ref. [32]. The reconstruction quality is influenced by the statistical fluctuation of $S2$ hit pattern, and depends on the $S2$ charge. The position resolution (Fig. 5) is estimated conservatively by taking the data-driven edge events ($S2$ from ^{210}Po alpha), by a series Gaussian fit on the radius distribution of different $S2_b$ ranges.

Non-functioning PMTs (“off-PMT”) lead to topological defects in the charge pattern on PMTs, leading to offsets in horizontal position reconstruction. Especially when several adjacent PMTs are malfunctioning, this offset effect becomes more pronounced, which results in significant charge loss. To reduce the reconstruction uncertainty at and close to “off-PMT” regions, the brightest PMT channel center is used as the prior position of the reconstructed algorithm. Relaxed $S2$ TBA selection criteria to the scatter events located at this region is applied to reduce the acceptance loss.

F. Model of signal reconstruction in signal response model

The PE waveforms, shaped by PMTs, undergo processing procedures described in the previous subsections. These detected hits are organized into clusters, which are further classified as either $S1$ or $S2$ signals based on their respective pulse widths. The identified $S1$ and $S2$ signals are subsequently paired together to form physical events. However, it is important to note that both $S1$ and $S2$ signals can be subject to biases during the clustering and classification processes. For example during the clustering process, the hits are assigned to clusters if the time difference between any two hits is less than 60 ns. Considering the photon propagation in LXe and reflection on PTFE surface, the efficiency loss caused by the clustering process could be non-trivial. This effect mainly influences the low-energy region, and the number of photons that survive the hit clustering is modeled as

$$N'_{\text{det}} = B(N_{\text{det}}, 1 - \varepsilon_{\text{hit}}), \quad (9)$$

where the ε_{hit} is the loss probability of 1 hit during the clustering and is dependant on the number of hit N_{det} , shown in Fig. 6. The hit loss probability is

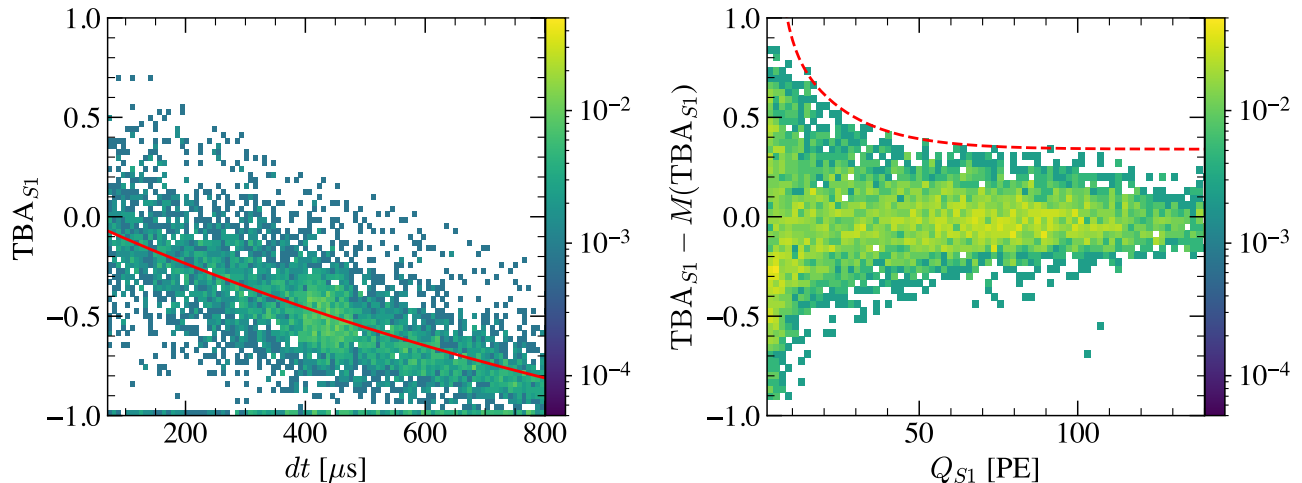


FIG. 4. Left: the distribution of low energy ER and NR calibration events presenting the relation between TBA_{S1} and drift time. The red solid curve illustrates the median of TBA_{S1} (ie. $M(TBA_{S1})$). Right: Median-centering for TBA_{S1} as a function of Q_{S1} . Any $S1$ above the red dashed curve is not treated as a major $S1$.

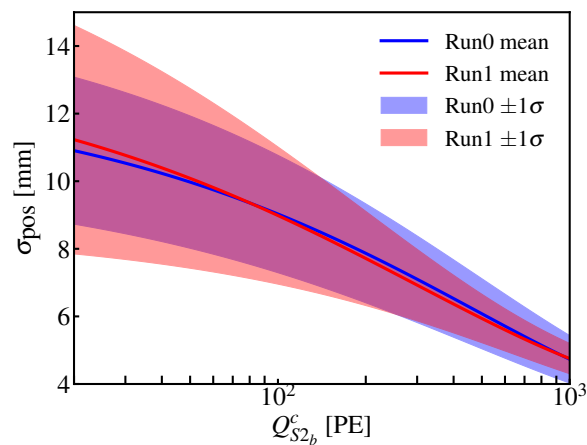


FIG. 5. Position reconstruction resolution as a function of the corrected $S2$ charge from bottom PMTs.

estimated using the PandaX-4T waveform simulation framework [31].

Furthermore, it is important to acknowledge the potential bias introduced to the $S1$ charge measurement due to the self-trigger threshold of the digitizers. The self-trigger threshold is set at 20 ADC, and as a result, single hits below this threshold will be discarded. Consequently, the $S1$ obtained after hit clustering may be underestimated compared to the true $S1$ value. Externally triggered data without such 20-ADC self-trigger threshold from the LED light calibration is utilized to determine the efficiency of such 20-ADC self-trigger threshold to $S1$ s with various signal sizes. Applying the self-trigger threshold allows for the successful recording of approximately 90% of the single

PEs, contributing to the overall bias in the $S1$ charge measurement. The $S1$ charge is modeled in the signal response model as

$$Q_{S1} = N_{PE}G(1 + \delta_{S1}^{\text{self}}, \Delta\delta_{S1}^{\text{self}}), \quad (10)$$

where $\delta_{S1}^{\text{self}}$ and $\Delta\delta_{S1}^{\text{self}}$ represent the $S1$ mean bias caused by the self-trigger and its associated fluctuation, respectively. The bias caused by the self-trigger threshold is overlaid in the left panel of Fig. 6.

The aforementioned factors also collectively contribute to a slight bias in the $S2$ charge after the signal reconstruction. The combined biases arising from the clustering, classification, and pairing procedures for the $S2$ signal (δ_{S2}), along with their corresponding fluctuation ($\Delta\delta_{S2}$), are assessed through a dedicated waveform simulation, as detailed in Ref. [31]. Fig. 6 illustrates the mean and fluctuation of these biases for $S2$ signals as a function of the $S2$ charges. The $S2$ charge (Q_{S2}) is then modelled as:

$$Q_{S2} = N_{\text{prop}}G(1 + \delta_{S2}, \Delta\delta_{S2}), \quad (11)$$

Signal reconstruction can also contribute to a direct loss in efficiency, particularly during the processes of pulse classification and the pairing of $S1$ and $S2$ signals. The assessment of these efficiencies is performed using the waveform simulation framework [31]. Efficiency values, characterized as a function of energy, are presented in Fig. 15.

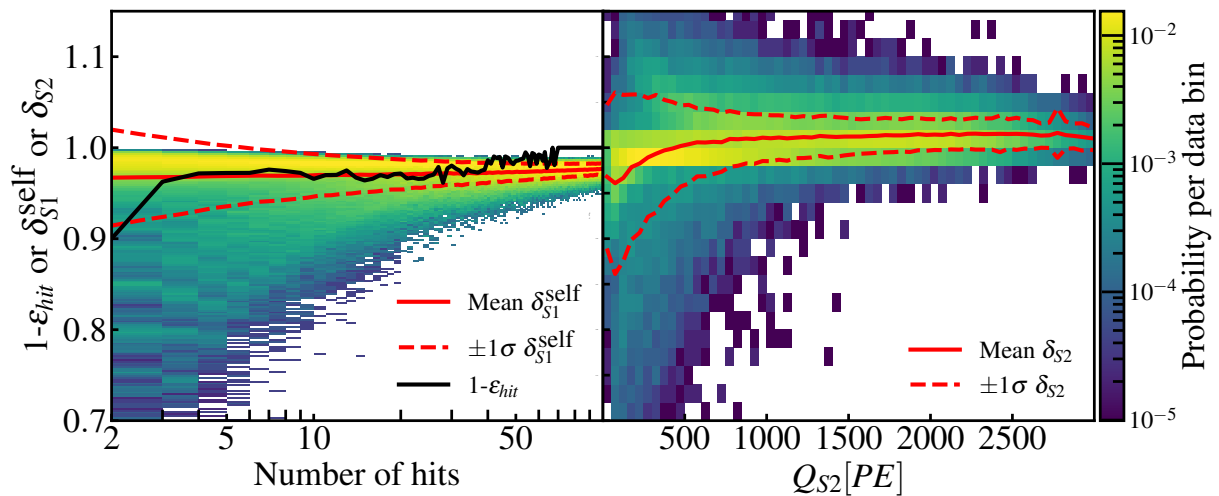


FIG. 6. The hit surviving probability $1-\varepsilon_{\text{hit}}$ is shown in left panel in black solid line, along with the probability distribution of self-trigger bias as a function of number of hit for the $S1$. In the right panel, it shows the probability distribution of $S2$ mean bias as a function of $S2$ charge Q_{S2}^e . The red solid and dashed lines display the mean and $\pm 1\sigma$ of the contour, respectively, in both panels.

V. SIGNAL CORRECTION

A. Spatial uniformity correction

The spatial non-uniformity of the $S1$ and $S2$ signals in the PandaX-4T detector is primarily attributed to several factors. These include the unevenness of the electric field, the levelness of the liquid-gas surface, and the optical solid angle. Additionally, operational conditions of the PMTs and impurity concentration in the LXe can also contribute to these non-uniformities. These spatial non-uniformities have the potential to degrade the energy resolution of the detector, thereby impacting its overall detection sensitivity. To correct for the spatial non-uniformities, a method utilizing an injected radioactive source, specifically $^{83\text{m}}\text{Kr}$, is employed. It is assumed that the 41.5 keV X-ray-induced ER events from $^{83\text{m}}\text{Kr}$ are uniformly distributed throughout the sensitive volume of the PandaX-4T TPC. The correction maps, expressed as the photon detection efficiency ε_{PDE} and charge amplification factor κ_b for $S1$ and $S2_b$, respectively, are obtained through a fitting procedure using a three-variable 9th-degree polynomial function ($\sum_{ijk} c_{ijk} x^i y^j z^k$, where i, j, k are integers from 0 to 9). Fig. 7 shows the ε_{PDE} on (r^2, z) and (x, y) for Run0 and Run1. Fig. 8 shows κ_b on (x, y) for Run0 and Run1. The reconstructed positions in $^{83\text{m}}\text{Kr}$ data are approximated as the true positions since the position reconstruction resolution is small at the $S2$ size for $^{83\text{m}}\text{Kr}$ (>1000 detected electrons).

As mentioned in Sec. III, the number of electrons gets reduced due to the attachment to electro-negative impurities in LXe during the drift process. The 5.6 MeV ^{222}Rn α events are also used for obtaining the electron

lifetime τ_e . All physical $S2$ s adopt this z -dependent charge correction by a factor of $e^{-z/\tau_e/v_{\text{drift}}}$.

B. Temporal variation correction

The magnitude of the detected $S1$ and $S2$ signals in the PandaX-4T experiment is known to be affected by variations in the detector conditions, such as the liquid level. These variations occur over time, particularly during Run1 when the overflow tube experienced a failure. To mitigate the impact of this instability, a temporal correction is applied to the $S1$ and $S2$ signals. To derive the run-by-run time-correction factors for the $S1$ and $S2$ signals, 5.6 MeV α decay events from ^{222}Rn are utilized. These events are used to determine the correction factors, which are then applied to signals at all energy levels. Only ^{222}Rn α events with drift times ranging from 200 μs to 550 μs are considered. The lower and upper limits of the drift time range are set to avoid influences from other radioactive impurities and PMT saturation, respectively. The reference points for the correction factors are determined based on the average values of the last 10 DM runs for both Run0 and Run1. Set 1-3 of Run0 are further corrected set-by-set based on the 163.9 keV γ peak from $^{131\text{m}}\text{Xe}$ in a similar approach. The variations before such temporal correction are 0.6%(0.7%) in $S1$ and 1.6%(4.6%) in $S2_b$ on average for Run0(Run1).

C. Position correction

Due to several detector effects including the distortion of drift electric field and the segmented coverage of the

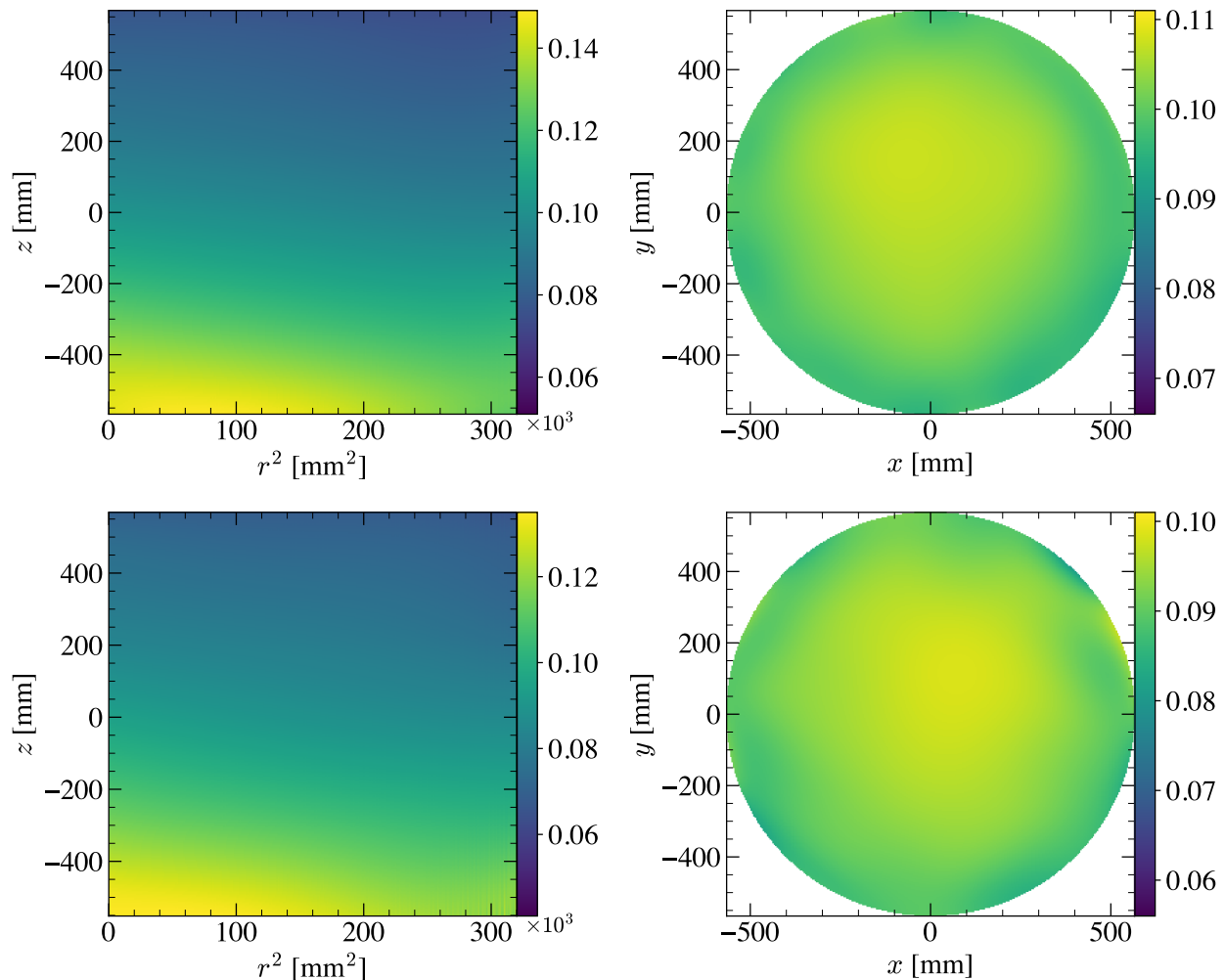


FIG. 7. The 3-D PDE ε_{PDE} map projected on (r^2, z) and (x, y) planes are shown in the left and right panels, respectively. The top and bottom panels show the maps for Run0 and Run1, respectively. The color axes give the values of the position-dependent PDE $\varepsilon_{\text{PDE}}(x, y, z)$ (Eq. 3).

top PMTs, events, especially for those close to the PTFE wall, tend to be reconstructed towards the interior in terms of horizontal position. For a direct comparison in the MC simulation, an azimuth-angle-dependent as well as z-dependent horizontal radial position affine scaling is necessary. The scaling factors are derived based on the uniformity of $^{83\text{m}}\text{Kr}$ ER events. Fig. 9 shows the significant effect of this radial scaling using ^{210}Po α events, which are mostly from the PTFE surface and selected through dedicated criteria involving event's $S1$ charge and TBA.

D. Model of signal correction in signal response model

In the PandaX-4T TPC, both the $S1$ and $S2$ signals exhibit spatial dependence, as discussed in previous

subsections. To account for the spatial dependence of signals, the $S1$ and $S2$ charges can be corrected through:

$$\begin{aligned} Q_{S1}^c &= Q_{S1} \langle \varepsilon_{\text{PDE}} \rangle / \varepsilon_{\text{PDE}}(x_{\text{rec}}, y_{\text{rec}}, z_{\text{rec}}), \\ Q_{S2}^c &= Q_{S2} e^{z/\tau_e / \nu_{\text{drift}}} \langle \kappa \rangle / \kappa(x_{\text{rec}}, y_{\text{rec}}). \end{aligned} \quad (12)$$

It should be noted that the position coordinates in Eq. 12 are the reconstructed coordinates. These reconstructed coordinates are susceptible to fluctuations due to the inherent resolution limitations of the position reconstruction algorithms. The extent of these fluctuations is influenced by the size of the $S2$ signal, with smaller $S2$ signals resulting in more pronounced fluctuations. The $S2$ -dependent position reconstruction resolution, denoted as σ_{pos} , is illustrated in Fig. 5. Assuming identical position resolutions in the x and y directions, the reconstructed transverse positions x_{rec}

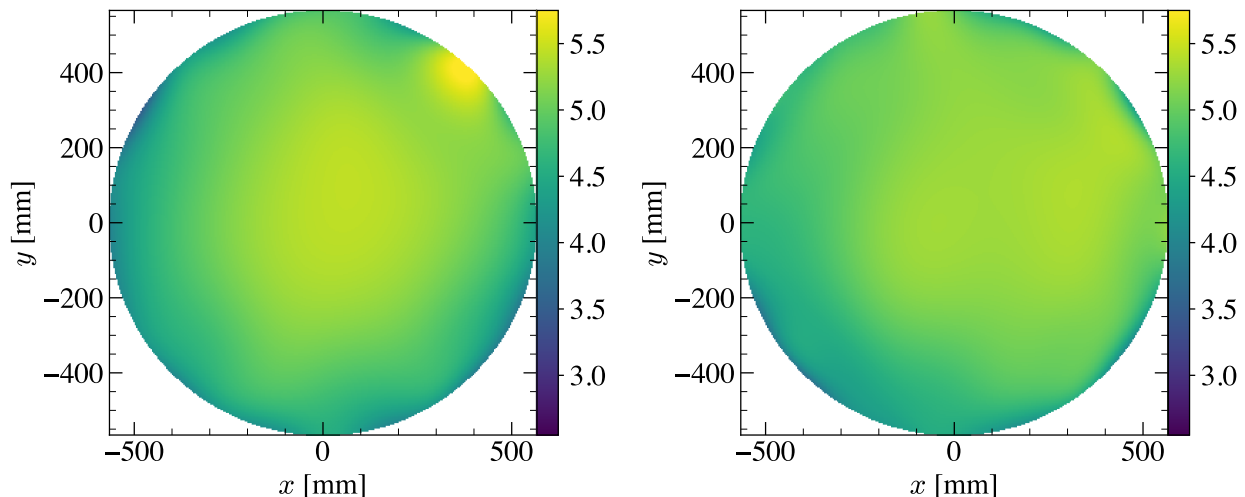


FIG. 8. The $S2$ gain maps as a function of horizontal position (x, y) for Run0 and Run1. The bright spot that appears in the right top of the left plot is due to one noisy PMT channel during Run0.

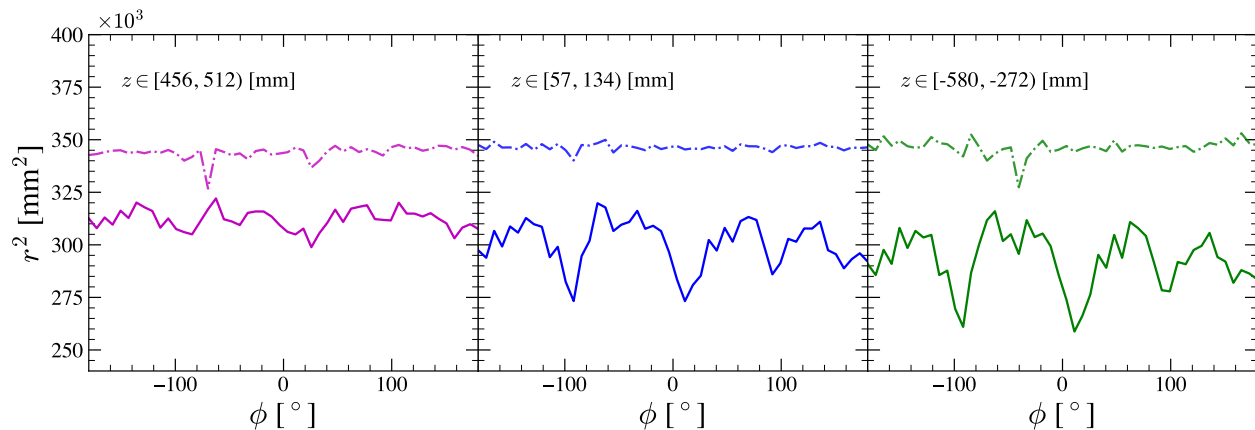


FIG. 9. The median of radius square of ^{210}Po α events before (solid line) and after (dash-dotted line) the azimuth-angle-dependent scaling at different z .

and y_{rec} can be expressed as

$$x_{\text{rec}} = G(x, \sigma_{\text{pos}}), y_{\text{rec}} = G(y, \sigma_{\text{pos}}). \quad (13)$$

VI. SIGNAL SELECTION

In order to maintain a high level of data purity and eliminate spurious events, a series of data selections are applied. These selections involve quality assessments of the $S1$ and $S2$ signals, correlation between $S1$ and $S2$, waveform “dirtiness”, and other considerations. More details are given in the following subsections.

A. Data quality

To ensure data quality in the PandaX-4T experiment, certain measures are implemented to remove exposure times that exhibit high rates of either $S1$ or $S2$ signals. The first step involves identifying and removing data files, each containing approximately 15 seconds of data, that exhibit significantly higher rates of $S1$ signals within a continuous period of time where the $S1$ rate exceeds the normal rate (10 to 15 Hz) by 2 standard deviations (2 to 3 Hz). 1% and 7% of live time are removed in Run0 and Run1, respectively. A specific treatment is applied to address the issue of afterglow, which refers to the presence of delayed electrons following a large signal. This treatment is performed on an event-by-event basis. After each pulse with a charge exceeding 10000 PE, a certain length of the recorded data time window is

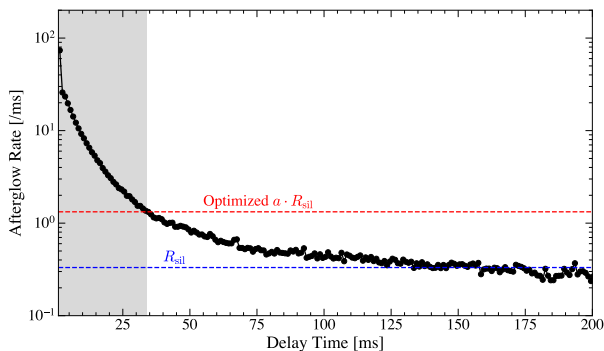


FIG. 10. An example of the $S2$ afterglow rate as a function of the delay time following one large $S2$ is shown by the black dots. The blue dashed line represents the calculated “silent rate” level. The red dashed line corresponds to the optimized cut-off rate $a \cdot R_{\text{sil}}$. The gray shaded region gives the time window for cut-off, which is determined based on the cut-off rate.

vetoed and excluded from analysis. To determine the appropriate length of the vetoed window, the concept of “silent rate” is introduced. The silent rate (R_{sil}) refers to the average rate of signals in non-vetoed windows, which are significantly delayed ($\gtrsim 200$ ms.) following large signals, within a given data file. The window length is determined such that the charge density (total $S2$ charge per unit time) falls below a threshold of $a \cdot R_{\text{sil}}$, as illustrated in Fig. 10. The scaling factor a is optimized by maximizing a figure-of-merit (FoM) defined as:

$$\text{FoM} = \frac{\epsilon_{\text{aft}}(a)}{\sqrt{R_{\text{aft}}(a)}}, \quad (14)$$

where ϵ_{aft} and R_{aft} are the fraction of exposure time left and average $S2$ rate, respectively, after applying the aforementioned veto on data time window. The exact value of a depends on the $S2$ ROI for the analysis which influences the values of R_{sil} and R_{aft} .

B. Individual signal quality

The reconstruction quality of individual physical signals is ensured by applying range selections on the parameters that are related to the $S1$ and $S2$ pulse shapes, as well as the signal distributions among PMTs. All the relevant parameters and their descriptions are listed in Table I. It’s worth noting that for events occurring near the PMTs that were turned off due to malfunctions (referred to as “off-PMT” region), the selection criteria based on TBA and reconstructed position parameters are appropriately relaxed to ensure that the acceptance in this region remains consistent with the rest of the TPC. The detail for signal quality selections on each parameter is presented in Fig. 11, showing the low-energy events distribution from the sum

of all the ^{220}Rn , $^{241}\text{AmBe}$ and DD calibration data in each specific parameter space, along with dashed colored lines represent the cut boundaries. The data points that deviate from the charge-dependent TBA_{S2} and fall below the lower boundary of the cut are associated with events that occur in the “off-PMT” region.

The efficiency of these individual signal quality selections are derived both from a data-driven approach using all of ^{220}Rn , $^{241}\text{AmBe}$ and DD calibration data and an approach based on the simulated samples from the waveform simulation [31], shown in Fig. 12. In the data-driven approach, the events in these low energy calibration data that pass the single scatter cuts (see Sec. VID) are selected to evaluate the efficiencies of the signal quality selections. Particularly, we require these events to have $S2$ charge and w_{CDF}^{90-10} values within 15%-85% (25%-75%) quantiles of the expected $S2$ charge and width distributions for NR (ER) calibration data to ensure the purity of the data sample. Considering the correlation between the selection criteria, efficiency of the selections that concern $S1$ -related ($S2$ -related) parameters are modeled as a function of Q_{S1} (Q_{S2}). The results of Run0 and Run1 are consistent with each other. The data-driven derived efficiency is taken as the nominal results, whilst the difference between waveform-simulation and data-driven results is considered as the systematic uncertainty.

C. $S1$ - $S2$ correlation

In liquid xenon detectors, ionized electron clusters experience a diffusion effect during their drift process. As a result, clusters with longer drift times will have larger widths, and specifically, the size in the vertical direction is reflected in the waveform’s width. In Fig. 13, we show the distributions of the CDF width w_{CDF}^{90-10} versus the drift time from the $^{83\text{m}}\text{Kr}$, ^{220}Rn , and neutron calibrations, as well as the α events from ^{222}Rn in the background data. Therefore a direct correlation between the primary width of the waveform and the drift time is established, known as the diffusion relation. Moreover, the broadening of the width distribution for smaller $S2$ s suffers more pronounced binomial fluctuations in the number of electrons contributing to the small signals. A charge-dependent selection criterion is applied on the normalized flattened parameter spaces of the 10%-to-90% (w_{CDF}^{90-10}) and 10%-to-50% (w_{CDF}^{50-10}) CDF widths. The flattening process reduces the dependence on the drift time. The distributions of the normalized flattened CDF widths $\mathcal{W}_{90} \equiv (w_{\text{CDF}}^{90-10} - M(w_{\text{CDF}}^{90-10}))/M(w_{\text{CDF}}^{90-10})$ and $\mathcal{W}_{50} \equiv (w_{\text{CDF}}^{50-10} - M(w_{\text{CDF}}^{50-10}))/M(w_{\text{CDF}}^{50-10})$, where M function gets the median of the variable from simulation, are displayed in Fig. 14. The parameter region between the 0.5% and 99.5% contours are selected.

The scintillation light can be generated anywhere in the sensitive volume and emit isotropically. A recoil taking place near the cathode/gate will collect more light

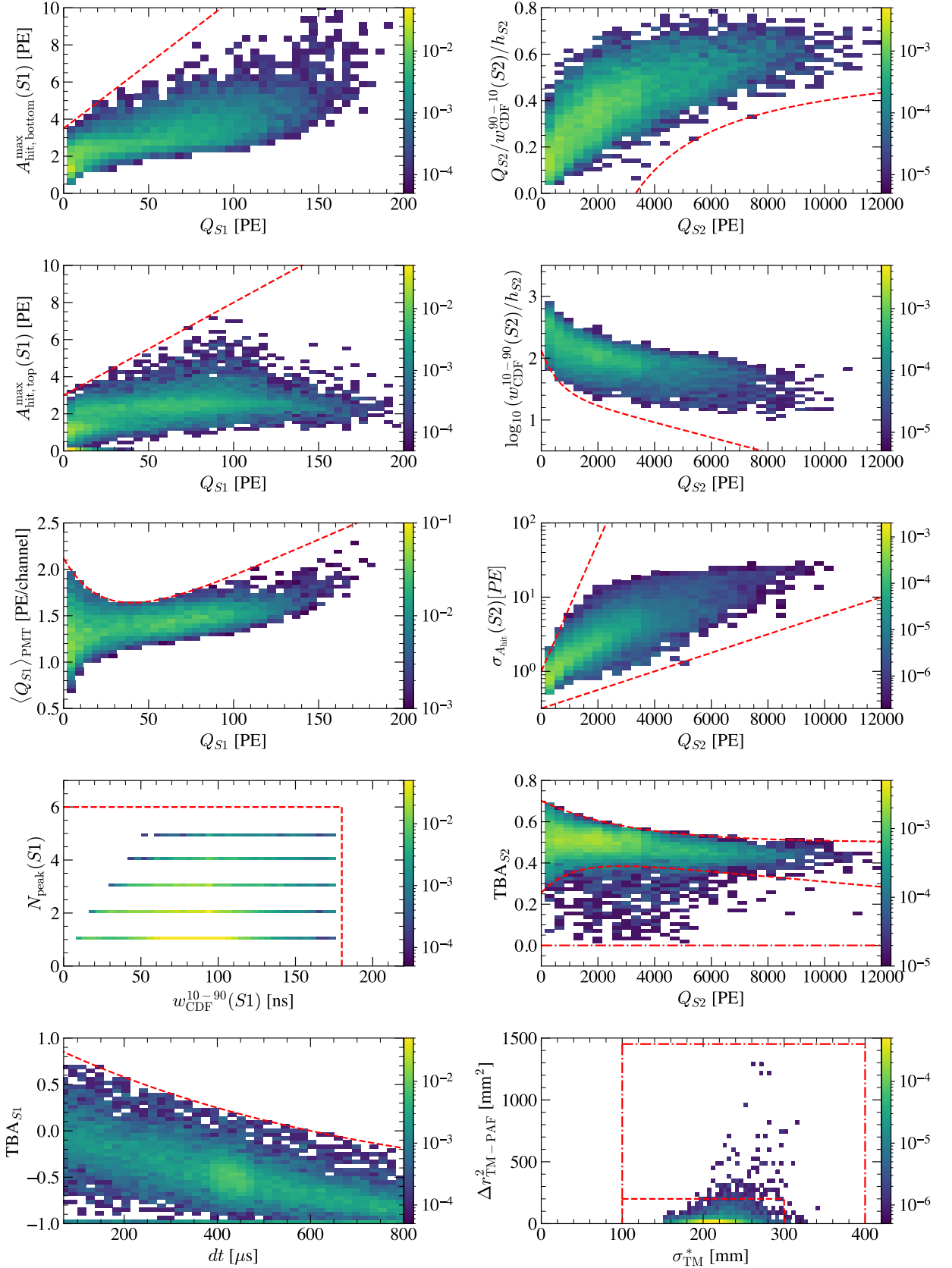


FIG. 11. The parameter spaces of all the $S1$ - and $S2$ -related quality selections. The data shown are the sum of all the ^{220}Rn , $^{241}\text{AmBe}$ and DD calibration data. The red dashed lines give the selection boundaries in each specific parameter space. The red dash-dotted lines indicate the relaxed selection boundaries for the “off-PMT” region. Table I describes the meaning of the variables used here.

Symbol	Description	Remarks for major noise
$A_{\text{hit,bottom}}^{\text{max}}(S1)$	The largest hit area at the bottom of $S1$	Remove sparking
$A_{\text{hit,top}}^{\text{max}}(S1)$	The largest hit area at the top of $S1$	Remove sparking
$\langle Q_{S1} \rangle_{\text{PMT}}$	The average charge per PMT channel of $S1$	Remove sparking
$N_{\text{peak}}(S1)$	The number of peaks identified in the $S1$ waveform	Remove $S1$ -like single electron
$w_{\text{CDF}}^{90-10}(S1)$	The CDF width of $S1$ waveform	Remove $S1$ -like single electron
TBA_{S1}	The TBA of $S1$	Remove accidental coincidence
$w_{\text{CDF}}^{90-10}(S2)$	The CDF width of $S2$ waveform	Remove accidental coincidence
h_{S2}	The height of $S2$ waveform	Remove sparking
$\sigma_{A_{\text{hit}}}$	The standard deviation of the hit areas of $S2$	Remove sparking
TBA_{S2}	The TBA of $S2$	Remove gas event
σ_{TM}^*	The charge-weighted standard deviation of the reconstructed position by TM algorithm	Poorly reconstructed position
$\Delta r_{\text{TM-PAF}}^2$	The square of the distance between two reconstructed positions by TM and PAF algorithms	Poorly reconstructed position

TABLE I. The parameters that are used in the signal quality selections, together with their descriptions and the types of noise they are intended to remove.

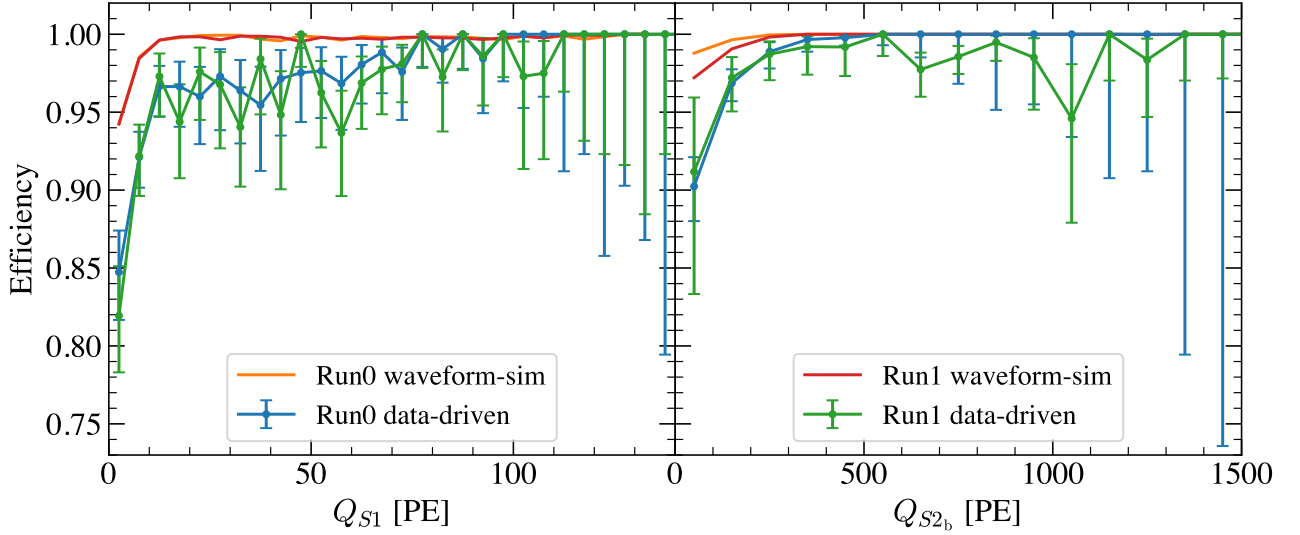


FIG. 12. Efficiency curves as functions of Q_{S1} and Q_{S2b} for $S1$ -related selection cuts and $S2$ -related selection cuts, respectively. The difference between waveform simulation and data-driven (see text for detailed description) results is considered to be a systematic uncertainty.

on the bottom/top PMT array due to the solid angle. Hence such a geometric relation of the scintillation light is illustrated by a selection cut in terms of $S1$ TBA as a function of the electron cloud drift time.

D. Single scatter

Neutrons generated through spontaneous fission and the (α, n) reaction of radioactive materials within the detector can undergo MS interactions within the sensitive volume. A crucial parameter for categorizing a single-scattering (SS) event is the count of $S2$ signals that meet specific quality selection criteria. Only $S2$ s with a full width greater than $0.8 \mu\text{s}$ that fall within certain

TBA parameter ranges for $S2$ will contribute to the count. To distinguish from the afterglow effect, any $S2$ signal that exhibits a charge value above a predetermined threshold is considered in the analysis

$$\begin{cases} Q_{S2,i} > 75 \text{ PE} \\ Q_{S2,i} > 0.06 Q_{S2,\text{max}} \end{cases}, \text{ for all } i, \quad (15)$$

where $Q_{S2,i}$ and $Q_{S2,\text{max}}$ are uncorrected charges of the i -th largest and the largest $S2$, respectively, in the event.

Besides, in order to further suppress the background due to the material neutrons, MS events with one interaction in the veto region are rejected. The veto region is between the inner vessel and TPC's PTFE side panel reflector. These MS events are identified as non-zero photo charges within the $S1$ window in the veto

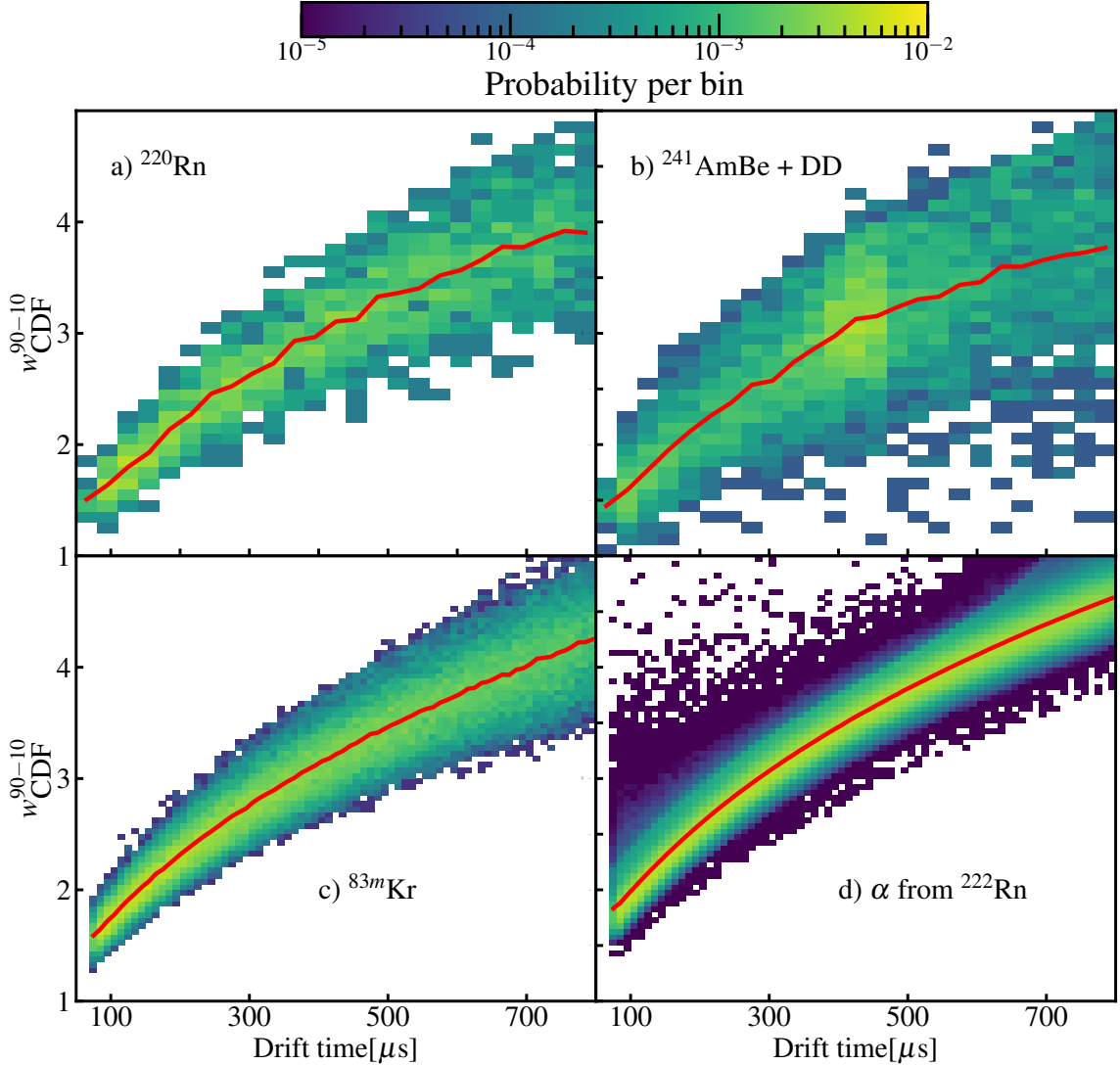


FIG. 13. The normalized distributions of the $S2$'s w_{CDF}^{90-10} over the drift time for four types of data: a) the ^{220}Rn calibration, b) the neutron calibration using $^{241}\text{AmBe}$ and DD, c) the $^{83\text{m}}\text{Kr}$ calibration, and d) the α events originated from ^{222}Rn impurities. The red solid lines represent the means of the distributions.

region, and excluded from the analysis. Approximately 20% of the neutron events are removed by this veto based on the neutron calibration data.

E. Waveform “dirtiness”

The actual recorded waveform in real data within an event time window contains not only the $S1$ signal induced by scintillation light and the $S2$ signal caused by electroluminescence from ionized electrons but also various noise signals. These noise signals originate from PMT dark counts, micro-discharges, delayed single-electron extractions, and so on, which can degrade the quality of physical signal reconstruction. Thus, each event must adhere to a basic duty cycle requirement

within the event time window. In order to reduce the interference of noise signals on the reconstruction of the waveform and charge amplitude of physical $S1$ and $S2$ signals, the proportion of physical signals with respect to the entire event total charge is required to reach a certain threshold. The noise level depends on the data taking status, leading to a different threshold of 72% and 59% for ER and NR calibration data, respectively. ER calibration data have an extra requirement that the charge proportion of nonphysical signals before the major $S2$ must be smaller than 6%, with respect to the entire event total charge. Furthermore, for WIMP search analysis, events with more than one $S1$ signals that can be paired with an $S2$ are removed to eliminate any ambiguity in pairing. The optimized pulse classification strategy for low energy analysis is not proper for $S1$ much

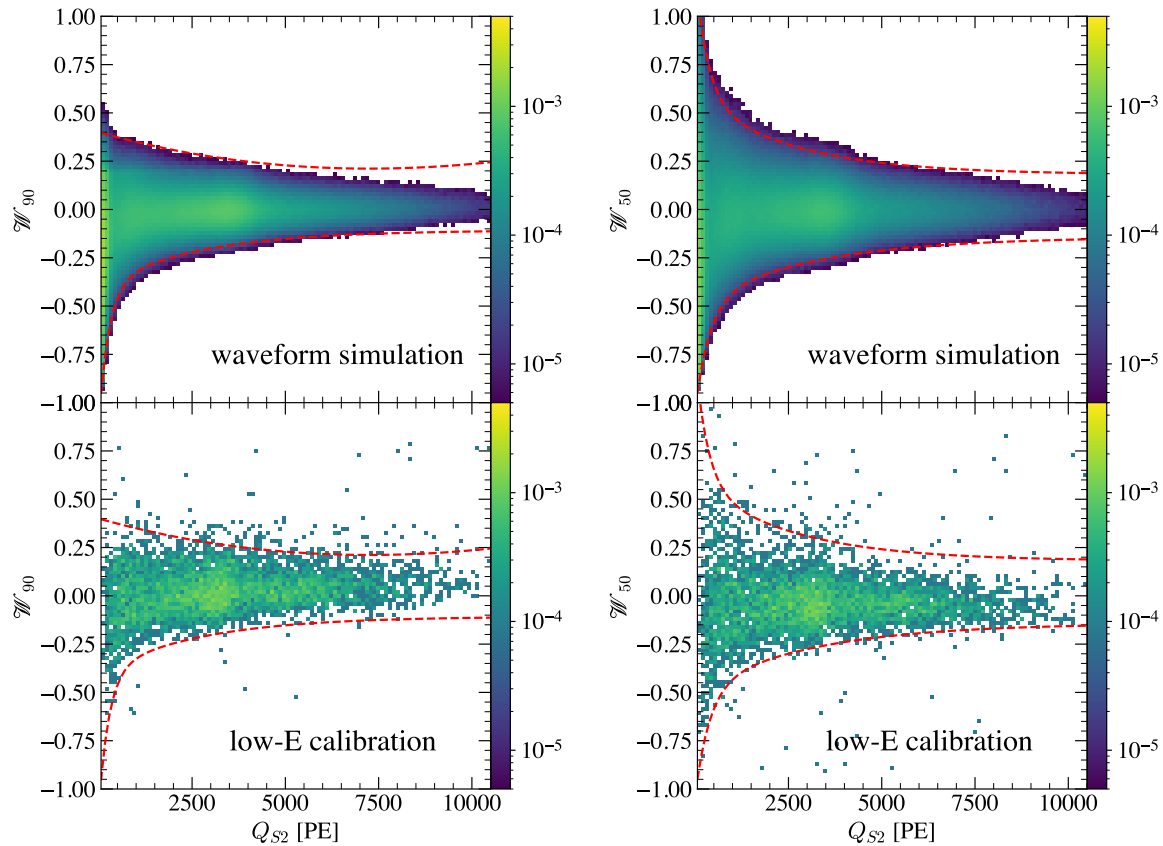


FIG. 14. The distributions of the normalized flattened CDF widths. The top and bottom panels give the distributions from the waveform simulation data and Run1 calibration data (^{220}Rn , $^{241}\text{AmBe}$ and DD), respectively. The left and right panels give the distributions of \mathcal{W}_{90} and \mathcal{W}_{50} , respectively. The red dashed lines indicate the selected parameter spaces.

greater than the low energy region of interest (> 500 PE), and it happens to be classified to a specific signal type called “Unknown”, which leads to its $S2$ wrongly paired with an small isolated $S1$. In order to specifically remove such events, the charge of all “Unknown” signal before the major $S2$ are required to be less than 4.2 times the charge of the mis-identified major $S1$.

F. Model of signal selection in signal response model

The efficiencies of the majority of these selections can be modeled as functions of the $S1$ or $S2$ signals. However, certain selections may also depend on additional variables, such as the drift time. For example, we require a correlation between the $S2$ width and drift time to satisfy the diffusion principle. For each simulated event in the signal response model, a weight w is assigned corresponding to its expected efficiency:

$$w = \epsilon_q \cdot \epsilon_r \cdot \epsilon_{\text{rec}} \cdot \epsilon_{\text{ss}}, \quad (16)$$

where ϵ_q and ϵ_r are the products of the quality data selections and the selections that require the $S1$ and $S2$ be in the ROI, respectively. ϵ_{rec} is the efficiency of signal reconstruction which is illustrated in Sec. IV. The single scatter selection efficiency is denoted as ϵ_{ss} . This selection requires that the largest $S2$ charge (Q_{S2}^{1st}) in an event is greater than a certain threshold value. The single scatter selection is a distinct data selection criterion designed to retain a majority of the genuine single scatter events while potentially misclassifying a portion of the true multiple scatter events as single scatters. Due to its unique nature, a simple efficiency measure is insufficient to fully characterize its impact on data purity. Thus, the SS selection is directly incorporated into the fast MC simulation of the signal response model. This enables the extraction of the $S1$ and $S2$ signal charges associated with each deposition cluster, providing a more accurate representation of the detector response to the GEANT4-simulated (G4-simulated) [33] event. In the case of $S1$ signals, their charges are combined since the simulated particles typically have sufficient speed, resulting in energy depositions occurring within a time frame shorter than the scintillation light propagation

time and the dimer decay constant. Unless the $S2$ signals of a particular simulated event satisfy the SS selection criteria given in Eq. 15, the efficiency ϵ_{ss} is set to 1 instead of 0. Additional details regarding the G4-based simulation and the clustering of energy depositions will be provided in Sec. VII.

VII. FIT TO DATA

The signal response model of PandaX-4T is tuned by matching the (Q_{S1}^c, Q_{S2b}^c) distributions between the calibration data and the fast-MC simulation. To expedite the fitting process, acceleration is employed for the simulation, leveraging the computational capabilities of GPUs. In this section, we provide a comprehensive description of the tuning process.

A. Calibration data

The tuning process of the PandaX-4T signal response model incorporates calibration data from three sources: injected ^{220}Rn source, external $^{241}\text{AmBe}$ neutron source, and a DD neutron generator. The total numbers of events used in fit are 1921 (2838), 1823 (935), and 1049 (1770) for ^{220}Rn , $^{241}\text{AmBe}$, and D-D calibration data, respectively, in Run0 (Run1). For the ^{220}Rn calibration, the energy spectrum is assumed to be “flat” in the low-energy region due to the dominant decay process of β decay from ^{212}Pb , which has a relatively high Q value of 584 keV. The spatial distribution of ^{212}Pb is also assumed to be uniform within the TPC, considering that several hours of data after injection has been removed to allow for sufficient diffusion. The $^{241}\text{AmBe}$ source is positioned outside the stainless steel container of PandaX-4T, at a radial distance of about 80 cm from the center of the PandaX-4T TPC. Three separate $^{241}\text{AmBe}$ runs are conducted with varying vertical positions of the source relative to the TPC center. This arrangement ensures neutron events are captured in the top, middle, and bottom regions of the PandaX-4T TPC. The emitted neutron energy spectrum from $^{241}\text{AmBe}$ is continuous, with the neutron energy ranging from several keV to a few MeV. In the case of the DD neutron generator, neutrons are transported from outside the water tank to the TPC through a stainless steel pipe surrounded by water during detector operation. DD calibration is performed with the generator tube oriented perpendicular to the stainless steel pipe, resulting in monoenergetic neutron energy of approximately 2.45 MeV.

B. GEANT4 simulation

The signal response model for NRs in PandaX-4T is tuned using neutron calibration data. Due to

the large size of the PandaX-4T TPC, neutrons have a considerable probability of undergoing multiple scattering within the detector. In the low-energy region, the selection efficiency for SS and the purity of rejecting MS are not optimal. Thus, the contribution of MS in the selected “SS” events is not negligible. To accurately model the contamination of MS, a dedicated simulation is conducted using the PandaX BambooMC framework [35] based on the GEANT4 toolkits [33]. Comparing the simulation result with NR calibration data, the relative difference is less than 8.5%. This simulation, referred to as the G4-based simulation in the manuscript, takes into account neutron propagation within the TPC. Furthermore, the capability of SS/MS discrimination is dictated by the z resolution in the TPC, which is determined by the complex signal reconstruction process, including clustering and $S2$ reclustering (as described in Sec. IV). The z resolution could depend on various factors such as the size and width of the $S2$ signal, as well as the position in the (x, y) plane. To incorporate these effects, a specific procedure is followed after the G4-based simulation. The simulated data are first subjected to a primary clustering algorithm that combines energy depositions with z positions closer than 0.5 mm. These primary energy clusters then are fed into waveform simulation [31], and subsequently undergo data reconstruction that is the same as used for real data. The resulting energy clusters for $^{241}\text{AmBe}$ and DD calibration data are utilized in the signal response model for model parameter fitting. Fig. 16 displays the total deposited energy spectra in the TPC for the $^{241}\text{AmBe}$ and DD calibration data. The neutron energies from the $^{241}\text{AmBe}$ source are associated with uncertainties, and additional deposit energy spectra are shown for alternative models with different initial neutron energy spectra, similar to [34]. Negligible differences in energy spectrum are observed. In the lower panel of Fig. 16, the 2-D distribution of the second largest energy versus the largest energy in the simulated data is also given. In addition, the end of the pipe used in DD neutron calibration stops a few centimeters away from the outer vessel wall of the cryostat. The thickness of this water layer has uncertainty due to the potential expansion of the water tank when fully loaded. The thickness is effectively determined to be approximately 6.25 cm through a primary matching of energy spectra between the G4-based simulation and the DD calibration data.

C. Parametrization in signal response model

The energy and field dependencies of key parameters of intrinsic light and charge generation in LXe for the signal response model are taken from the NESTv2 effective model, as described in Ref. [22]. These parameters include the excited-atom-to-ion ratio (α), the Lindhard factor for nuclear recoils (L), the initial mean recombination fraction ($\langle r \rangle_0$), and the initial

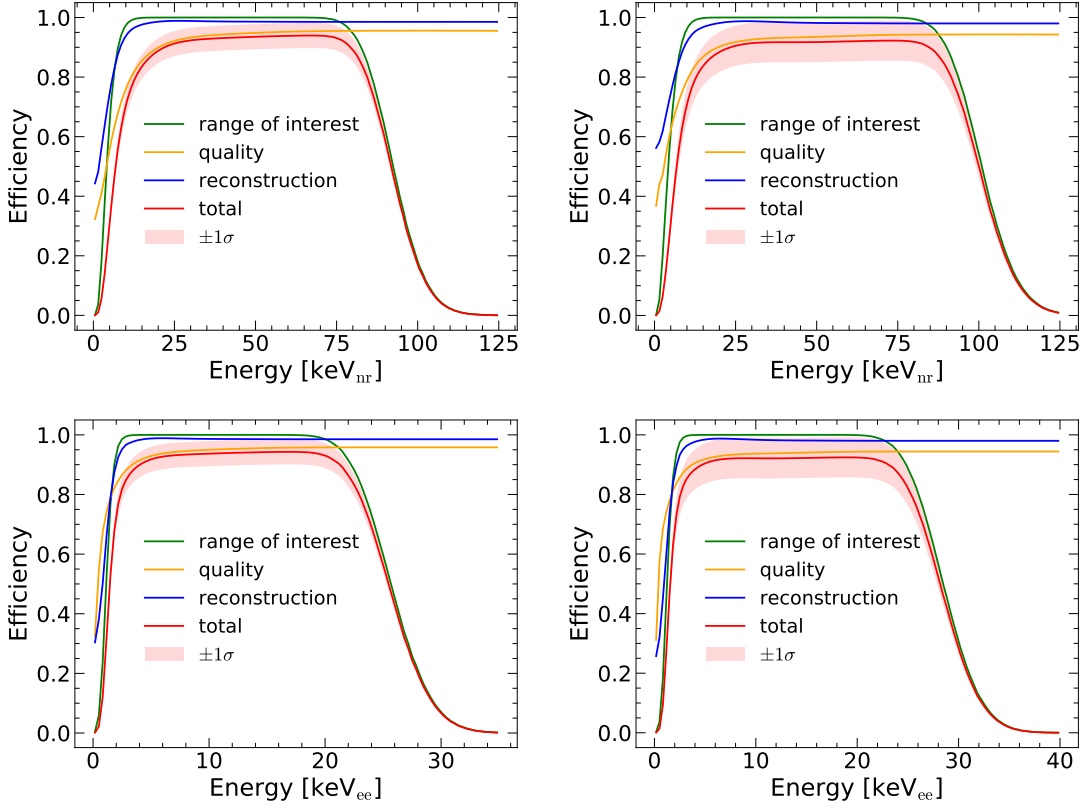


FIG. 15. The detection efficiency (green line), reconstruction efficiency (blue line), data quality efficiency (orange line), and the total efficiency (red, with the shaded band representing the uncertainty) as a function of NR energy (upper panels) and ER energy (lower panels). The left and right panels show the efficiencies for Run0 and Run1, respectively.

recombination fluctuation (Δr_0). The exact expressions used can be found in Appendix A.

The signal response model for ERs and NRs incorporates additional degrees of freedom for tuning the light and charge yields. Specifically, the mean recombination fraction $\langle r \rangle$ is adjusted by adding a 3rd-order Legendre polynomial P multiplied by an exponential function, and the recombination fluctuation Δr is scaled by a factor λ , respectively. The exponential function is applied to suppress the tuning in high-energy region, which is well understood with global measurements. Their dependence on the deposit energy ξ can be expressed as:

$$\begin{aligned}
 \langle r \rangle(\xi) &= \langle r \rangle_0(\xi) + P_3(\xi/\xi_{\text{norm}}; p_0, p_1, p_2, p_3) \cdot e^{-\xi/\xi_{\text{norm}}}, \\
 \Delta r(\xi) &= \Delta r_0(\xi) \cdot \lambda, \\
 \xi_{\text{norm}}^{\text{NR}} &= 30 \text{ keV}, \\
 \xi_{\text{norm}}^{\text{ER}} &= 150 \text{ keV},
 \end{aligned}
 \tag{17}$$

where p_0 , p_1 , p_2 , and p_3 are the coefficients of the 3rd-order Legendre polynomial function. The ξ_{norm} is the exponential constant, which are fixed for ERs and NRs, respectively. The orders of the Legendre polynomial functions are determined so that adding more degree of

freedom brings no significant improvement in data/model comparison. Independent sets of free parameters p_0 , p_1 , p_2 , p_3 , and λ are assigned to ER and NR. To compare the performance of the NESTv2 nominal model with the PandaX-tuned model (referred to as P4-NEST), we present the mean photon yields N_{ph}/ξ and charge yields N_e/ξ , along with the corresponding Δr , as functions of energy for both ER and NR. These results are depicted in Fig. 17.

D. Penalty constraints

The nuisance parameters employed to characterize the detector effect within the signal response model are acquired through independent studies and are associated with corresponding uncertainties. A comprehensive inventory of the free, constrained, and fixed parameters employed in the signal response model can be found in Table II. It is worth noting that a specific constraint is applied to the parameters g_1 and g_{2b} . The mean reconstructed energies for the three monoenergetic peaks ($^{83\text{m}}\text{Kr}$, $^{129\text{m}}\text{Xe}$, and $^{131\text{m}}\text{Xe}$) are required to closely align

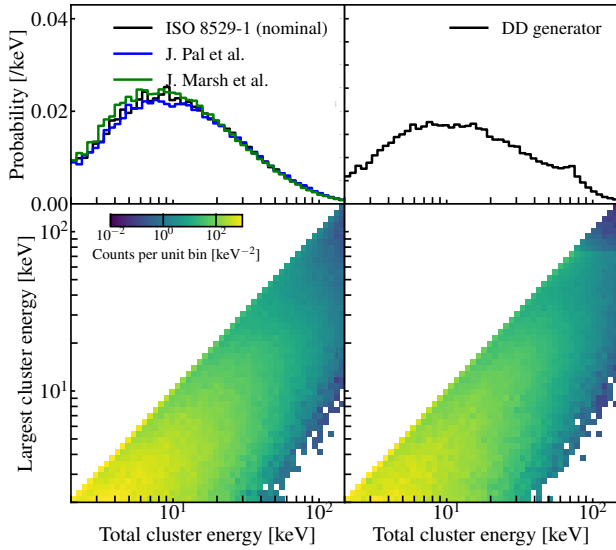


FIG. 16. The simulation outputs (energy deposition inside the FV) by GEANT4 toolkit are shown. The left and right panels display the simulation results for $^{241}\text{AmBe}$ source and DD generator, respectively. The top panels give the total deposit energy spectra, and the bottom panels display the distribution of the largest cluster energy over the total energy. The black lines are the nominal spectra used, while the blue and green solid lines are the alternative AmBe spectra from Ref. [34].

with their corresponding true energies:

$$\Lambda = \sum_i (E_{\text{rec},i} - E_{\text{tr},i})^2 / (2\sigma_{E_{\text{rec},i}}^2), \quad (18)$$

where i represents the index of the monoenergetic peak. $E_{\text{rec},i}$ and $E_{\text{tr},i}$ are the reconstructed (following Eq. 8) and true energies, respectively. $\sigma_{E_{\text{rec},i}}$ is the statistical uncertainty of the reconstructed energy following the error propagation $\sigma_{E_{\text{rec},i}} = W \sqrt{(\sigma_{cS1,i}/g1)^2 + (\sigma_{cS2b,i}/g2b)^2}$, where $\sigma_{cS1,i}$ and $\sigma_{cS2b,i}$ are the statistical uncertainties of the mean corrected signals Q_{S1}^c and Q_{S2b}^c for the i -th monoenergetic peak.

E. Contamination in the calibration data

Neutrons can scatter inelastically or be captured by atoms in material, resulting in the emission of high-energy gamma rays. As a consequence, neutron calibration data are contaminated by ER events. Additionally, intrinsic gamma rays are emitted alongside neutrons in the case of the $^{241}\text{AmBe}$ source. To account for these effects, we introduce one degree of freedom for the ratio of ER contamination to NR in each neutron calibration data. The energy spectrum of such ERs is assumed to be flat in low-energy region, since they are basically caused by small-angle Compton scatters

of MeV gamma rays. In Run0, we also have remnant tritiated methane during the ^{220}Rn calibration. A tritium β component with a constrained rate is added to the ^{220}Rn simulation in the parameter fitting, with total event of 14_{-0}^{+13} counts. The uncertainty is estimated as the difference between the tritium rates estimated using the background data taken during and before the ^{220}Rn calibration.

The accidental coincidence (AC) rate can increase in calibration data, particularly during neutron calibrations, due to high event rates. We estimate the AC rate and its spectral shape using the isolated $S1$ and $S2$ rates [14].

F. Combined fit to calibration data in Run0+Run1

The fit is performed by maximizing the likelihood function:

$$\mathcal{L} = \prod_{\alpha,\beta} \frac{\lambda_{\alpha\beta}^{N_{\alpha\beta}}}{N_{\alpha\beta}!} e^{-\lambda_{\alpha\beta}} \cdot e^{-\Lambda}, \quad (19)$$

where α and β represent the indices of the used calibration dataset and the data binning, respectively. In our analysis, the 2-D distribution of the Q_{S2b} over Q_{S1}^c is fit for tuning the signal model, with 30 bins for the $S1$ from 0 to 135 PE and 30 bins for the Q_{S2b} from 0 to 3000 PE by default. $\lambda_{\alpha\beta}$ and $N_{\alpha\beta}$ are the expectation and observed number, respectively, for β -th bin of the distribution from α -th calibration data. Λ is the constraint on the reconstructed energy which is given by Eq. 18. To optimize the likelihood, we employ the emcee toolkit [38], which utilizes Goodman & Weare's Affine Invariant Markov chain Monte Carlo Ensemble sampler [39]. During the optimization process, the expected values $\lambda_{\alpha\beta}$ are calculated using dedicated signal response simulation data with sufficient statistics. Specifically, for each iteration, we use a substantial number of events (default: 10^7 for ER calibration and 2×10^6 for NR calibration) to ensure accurate estimation. Due to this iteration-by-iteration simulation causing statistical fluctuation of the simulated samples, the likelihood is further corrected:

$$\mathcal{L}' = \mathcal{L} / \sqrt{1 + \sigma_{\mathcal{L}}^2}, \quad (20)$$

where $\sigma_{\mathcal{L}}$ is the relative statistical fluctuation of the likelihood which is typically 1-2 for the ER and NR simulations with default MC statistics. They are updated every 500 iterations during the fitting.

A simultaneous fit of all the calibration data (^{220}Rn , $^{241}\text{AmBe}$, and DD calibration) in Run0 and Run1 was conducted[40]. The optimization process by emcee is determined to be converged when the Gelman-Rubin test statistics [41] drops below 1.1. The parameterization of $\langle r \rangle$ in Run1 is identical to those in Run0, except for that we consider there a constant difference between

Parameters	Description	Constrain	Nominal	Best-fit	Note & reference
p_{dpe}	Double-PE probability	fixed	0.22	-	(Eq. 4)
τ_e	Electron lifetime	fixed	-	-	Time dependent (Eq. 5, Fig. 1)
ϵ_{ext}	Electron extraction efficiency	fixed	-	-	Correlated with g_2 and κ (Eq. 6)
κ	Electron amplification factor	fixed	-	-	Time dependent (Eq. 7 & Fig. 2)
g_1	$S1$ gain	free	-	$0.0997^{+0.0002}_{-0.0005}$	Extra constraint on reconstructed energy (Eq. 8 & Sec. VIID)
g_{2b}	$S2$ gain	free	-	$4.12^{+0.06}_{-0.04}$	
f_{g1}	Scale factor of $S1$ gain in Run1	fixed	0.90985	-	$S1$ dependent (Eq. 9 & Fig. 6)
f_{g2b}	Scale factor of $S2$ gain in Run1	fixed	1.22067	-	$S1$ dependent (Eq. 10 & Fig. 6)
ϵ_{hit}	Loss probability of 1 hit due to clustering	fixed	-	-	
δ_{S1}^{self}	self-trigger bias on $S1$	fixed	-	-	
$\Delta\delta_{S1}^{self}$	Standard deviation of self-trigger bias	fixed*	-	-	
δ_{S2}	Mean $S2$ reconstruction bias	fixed	-	-	
$\Delta\delta_{S2}$	Standard deviation of reconstruction bias	fixed*	-	-	
σ_{pos}	Position reconstruction resolution	fixed	-	-	$S2$ dependent (Eq. 11 & Fig. 6)
ϵ_q	Quality cut efficiency	fixed	-	-	$S2$ dependent (Eq. 13 & Fig. 5)
ϵ_r	ROI efficiency	fixed	-	-	Depend on various variables (Eq. 16 & Fig. 15)
ϵ_{rec}	Signal reconstruction efficiency	fixed	-	-	Depend on various variables (Eq. 16 & Fig. 15)
ϵ_{ss}	Single scatter cut efficiency	fixed	-	-	Special implementation in fast MC (Sec. VI)
p_{ER}		free	-	1.1 ± 0.4	
p_{UR}		free	-	-3.1 ± 1.2	
p_{2ER}		free	-	$2.2^{+0.6}_{-0.8}$	
p_{2UR}		free	-	$-1.7^{+0.7}_{-0.6}$	
p_{3ER}		free	-	0.7 ± 0.3	
p_{NR}		free	-	$-1.6^{+0.9}_{-0.7}$	
p_0		free	-	$1.3^{+0.5}_{-0.7}$	
p_1		free	-	-0.6 ± 0.4	
p_2		free	-	$1.11^{+0.06}_{-0.04}$	
p_3		free	-	$1.06^{+0.09}_{-0.10}$	
A_{ER}		free	-	0.031 ± 0.011	
A_{NR}		free	-	$0.028^{+0.016}_{-0.010}$	(Sec. VII E)
$R_{ER}^{AmBe,Run0}$	Recombination fluctuation scaling for ER	free	-	$0.029^{+0.016}_{-0.014}$	(Sec. VII E)
$R_{ER}^{AmBe,Run1}$	Recombination fluctuation scaling for NR	free	-	$0.029^{+0.008}_{-0.012}$	(Sec. VII E)
$R_{ER}^{DD,Run0}$	Ratio of ER contamination to NR in Run0 AmBe	constrained	0.007 ± 0.006	$0.010^{+0.006}_{-0.004}$	
$R_{ER}^{DD,Run1}$	Ratio of ER contamination to NR in Run1 AmBe	fixed	0.0038	-	
$R_{ER}^{Rn,Run0}$	Ratio of ER contamination to NR in Run0 DD	fixed	0.0076	-	
$R_{ER}^{Rn,Run1}$	Ratio of ER contamination to NR in Run1 DD	fixed	0.0021	-	
$R_{AC}^{AmBe,Run0}$	Ratio of Tritium's contamination in Run0 Rn	fixed	0.0044	-	
$R_{AC}^{AmBe,Run1}$	Ratio of AC contamination to NR in Run0 AmBe	fixed	-	$-0.032^{+0.004}_{-0.004}$	
$R_{AC}^{DD,Run0}$	Ratio of AC contamination to NR in Run1 AmBe	fixed	-	$-0.043^{+0.006}_{-0.007}$	(Sec. VII F)
$R_{AC}^{DD,Run1}$	Ratio of AC contamination to NR in Run0 DD	fixed	-	-	
d_{ER}	Recombination fraction shift for ER in Run1	free	-	-	
d_{NR}	Recombination fraction shift for NR in Run1	free	-	-	

TABLE II. Parameters of the combined fit with Run0 and Run1.

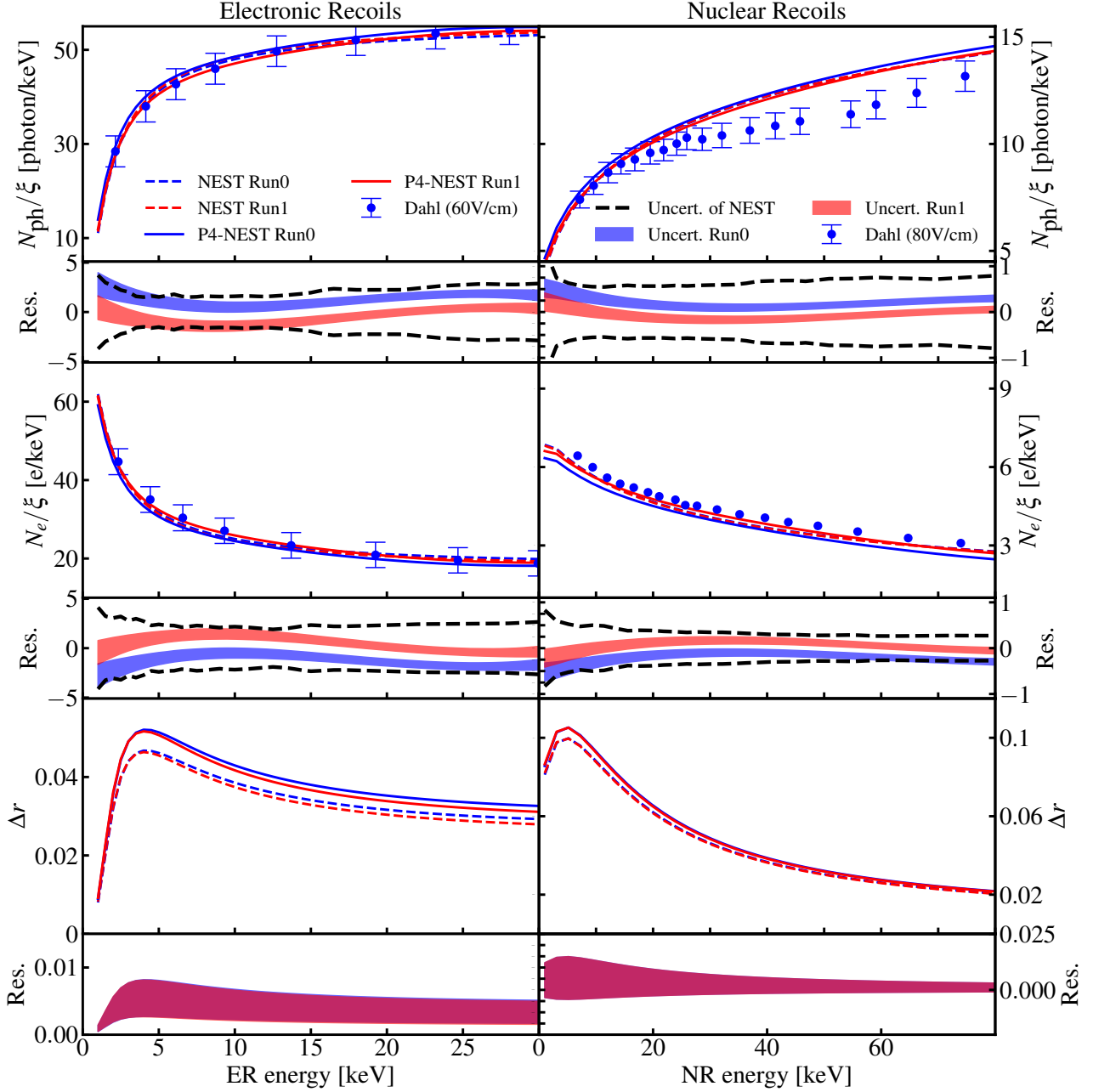


FIG. 17. The light yield, charge yield, and recombination fluctuation Δr as a function of the deposit energy are shown in the top, middle, and bottom panels, respectively. The left and right panels correspond to the results for ER and NR, respectively. The blue and red lines give the corresponding results for Run0 and Run1 electric field configurations. The dashed and solid lines represent the nominal predictions from NESTv2 [22] and the tuned results in this analysis. Small panels beneath each major panels give the uncertainty bands of the residual difference between the tuned results and nominal NEST prediction. The black dashed lines indicate the $\pm 1\sigma$ uncertainties of the nominal NEST predictions. We also show the light and charge yield measurements from Eric Dahl [36, 37] with the electric fields of 60 and 80 V/cm.

the $\langle r \rangle$ values of Run1 and Run0. This difference is introduced to accommodate the slightly different electric field conditions experienced during Run0 and Run1 in the sensitive regions of the experiment. Regarding the recombination fluctuation Δr , it is assumed to have a weak dependence on the electric field. Therefore, the

field dependency modeled in NESTv2 [22] is directly adopted for Δr . All fixed parameters associated with the detector effects, as discussed in previous sections, have been updated for Run0+Run1 combined fit and are listed in Table II. As described in Section III, the values of g_1 and g_{2b} in Run1 were found to exhibit slight deviations

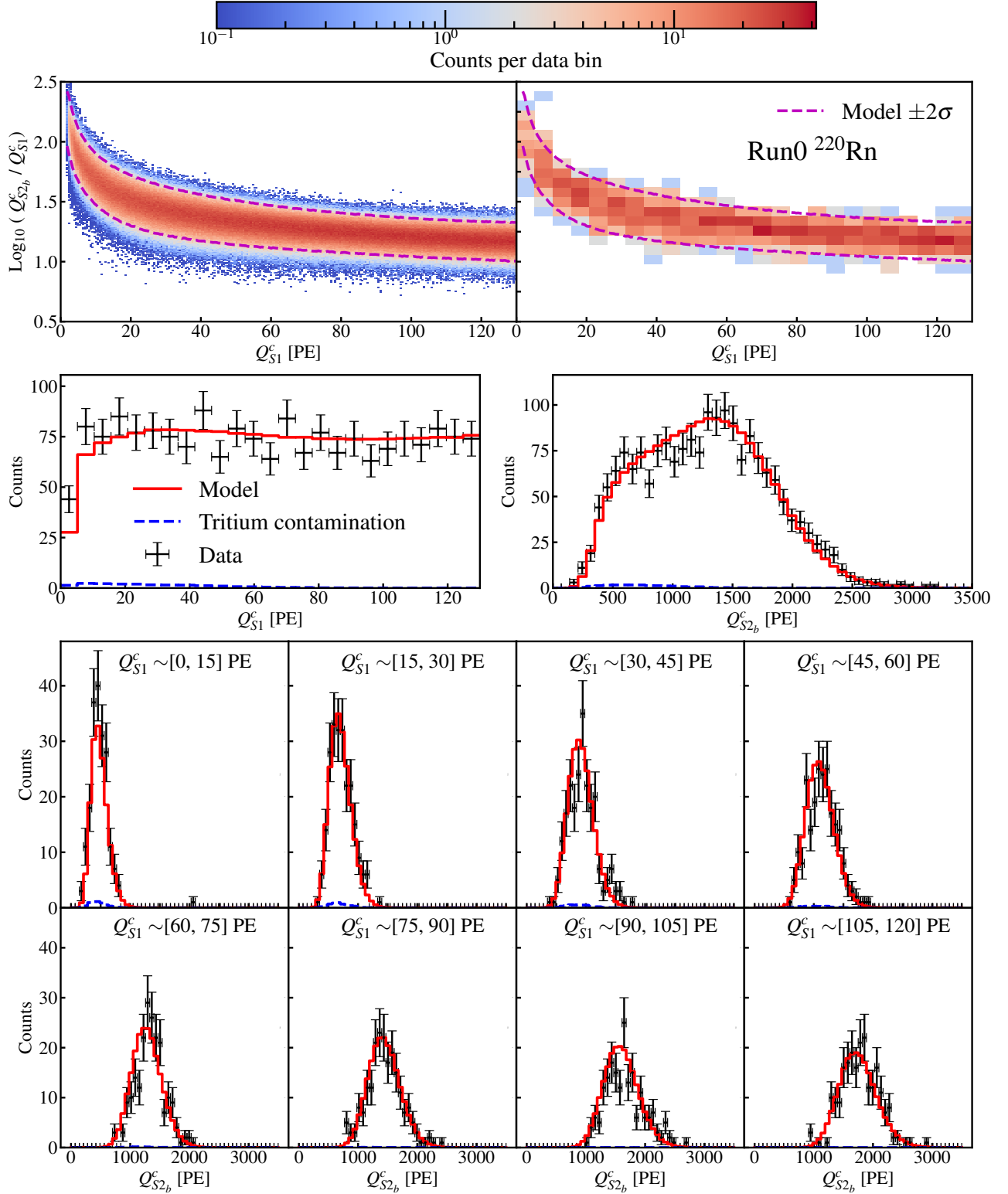


FIG. 18. The comparison between ^{220}Rn calibration data in Run0 and best-fit results of P4-NEST model from the simultaneous fit using Run0 and Run1 data. The top panels show the distribution of $\text{Log}_{10}(Q_{S2b}^c/Q_{S1}^c)$ over Q_{S1}^c for the P4-NEST model (left) and the data (right). The magenta dashed lines encircle the $\pm 2\sigma$ region of the NR from the P4-NEST model. The middle panels give the Q_{S1}^c and Q_{S2b}^c spectra from the data (black error bars) and the P4-NEST model (red solid lines), respectively. Blue dashed lines represent the contribution of the residual tritium impurities in the calibration run. The lower eight panels give the Q_{S2b}^c spectra in different Q_{S1}^c ranges.

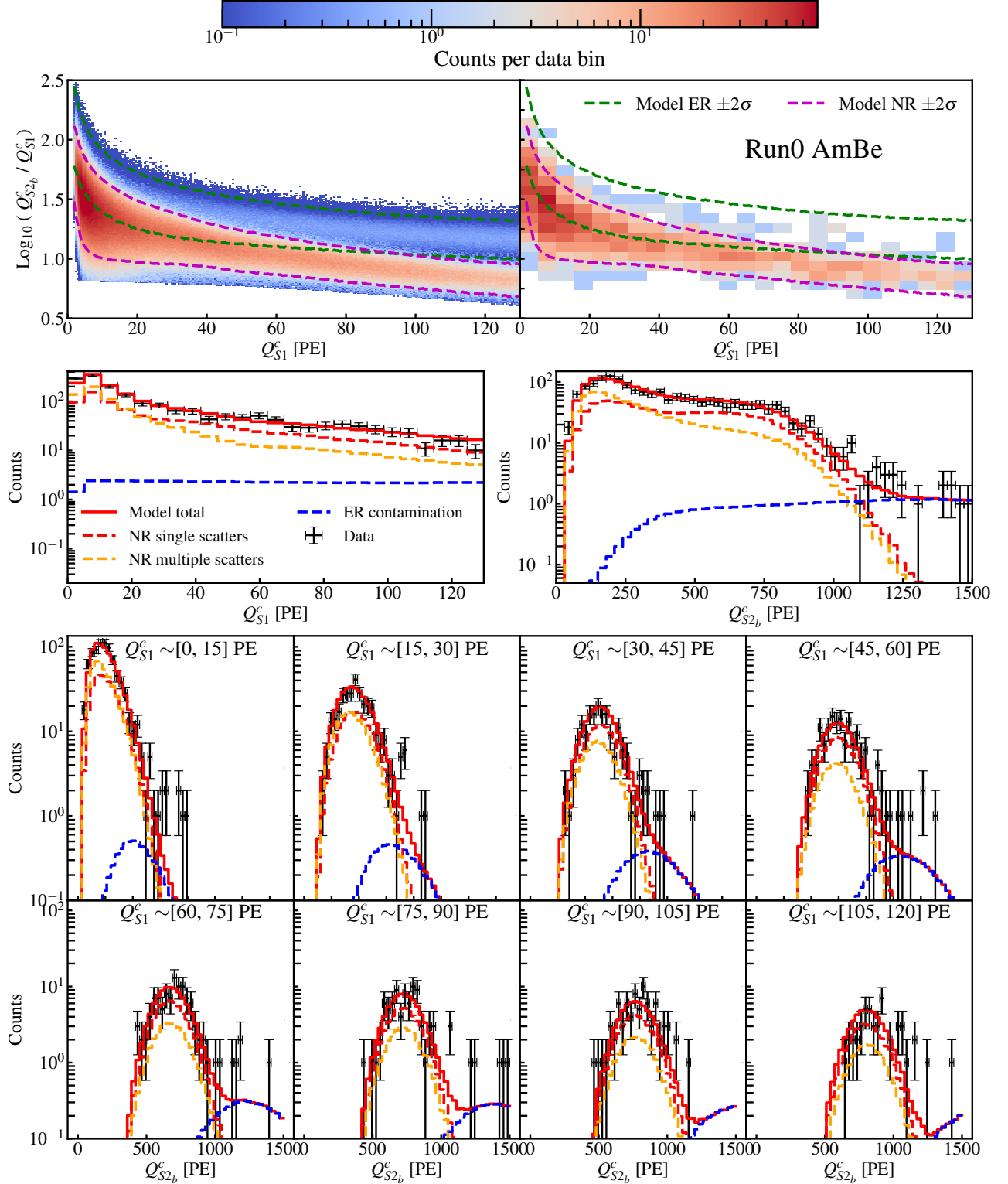


FIG. 19. The comparison between $^{241}\text{AmBe}$ neutron calibration data in Run0 and best-fit results of P4-NEST model from the simultaneous fit using Run0 and Run1 data. The figure layout and the line denotations are the same as Fig. 18. The green dashed lines are the $\pm 2\sigma$ boundaries of the ER from P4-NEST. The red, orange, and blue dashed lines in the middle and bottom panels are the model spectra of SS NR, MS NR, and ER contamination in the neutron calibration, respectively.

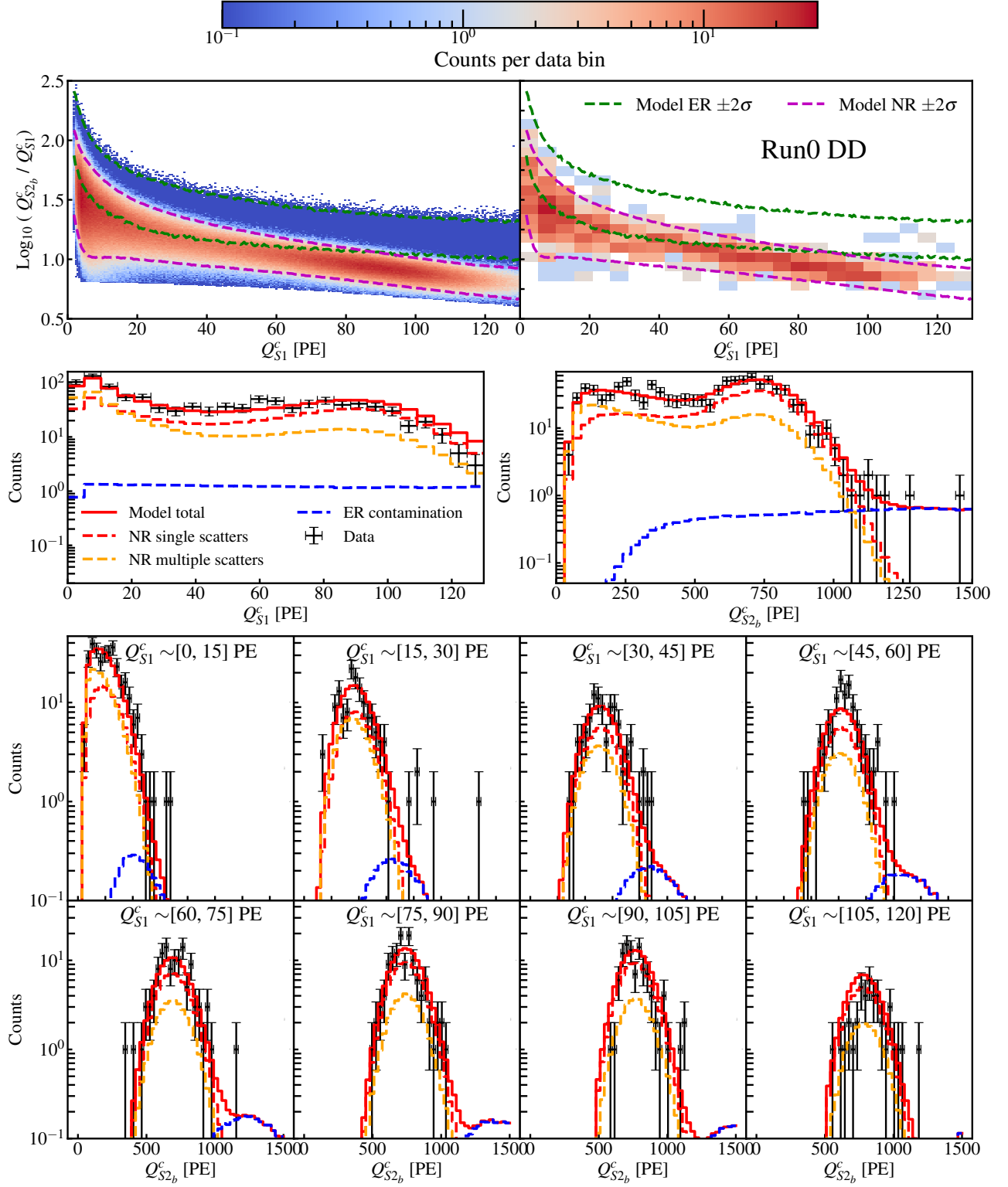


FIG. 20. The comparison between DD neutron calibration data in Run0 and best-fit results of P4-NEST model from the simultaneous fit using Run0 and Run1 data. The figure layout and the line denotations are the same as Fig. 19.

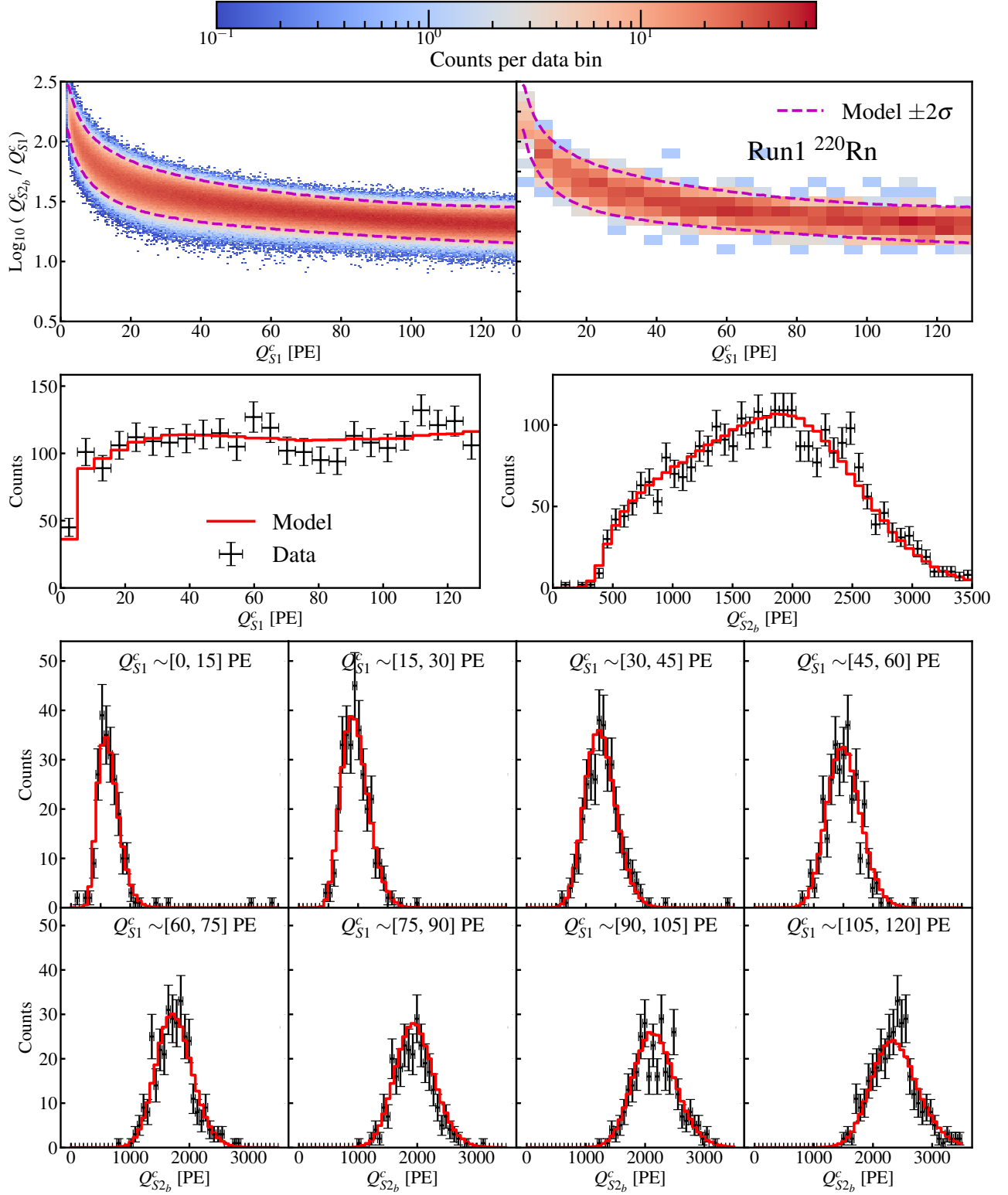


FIG. 21. The comparison between ^{220}Rn calibration data in Run1 and best-fit results of P4-NEST model from the simultaneous fit using Run0 and Run1 data. The figure layout and the line denotations are the same as Fig. 18.

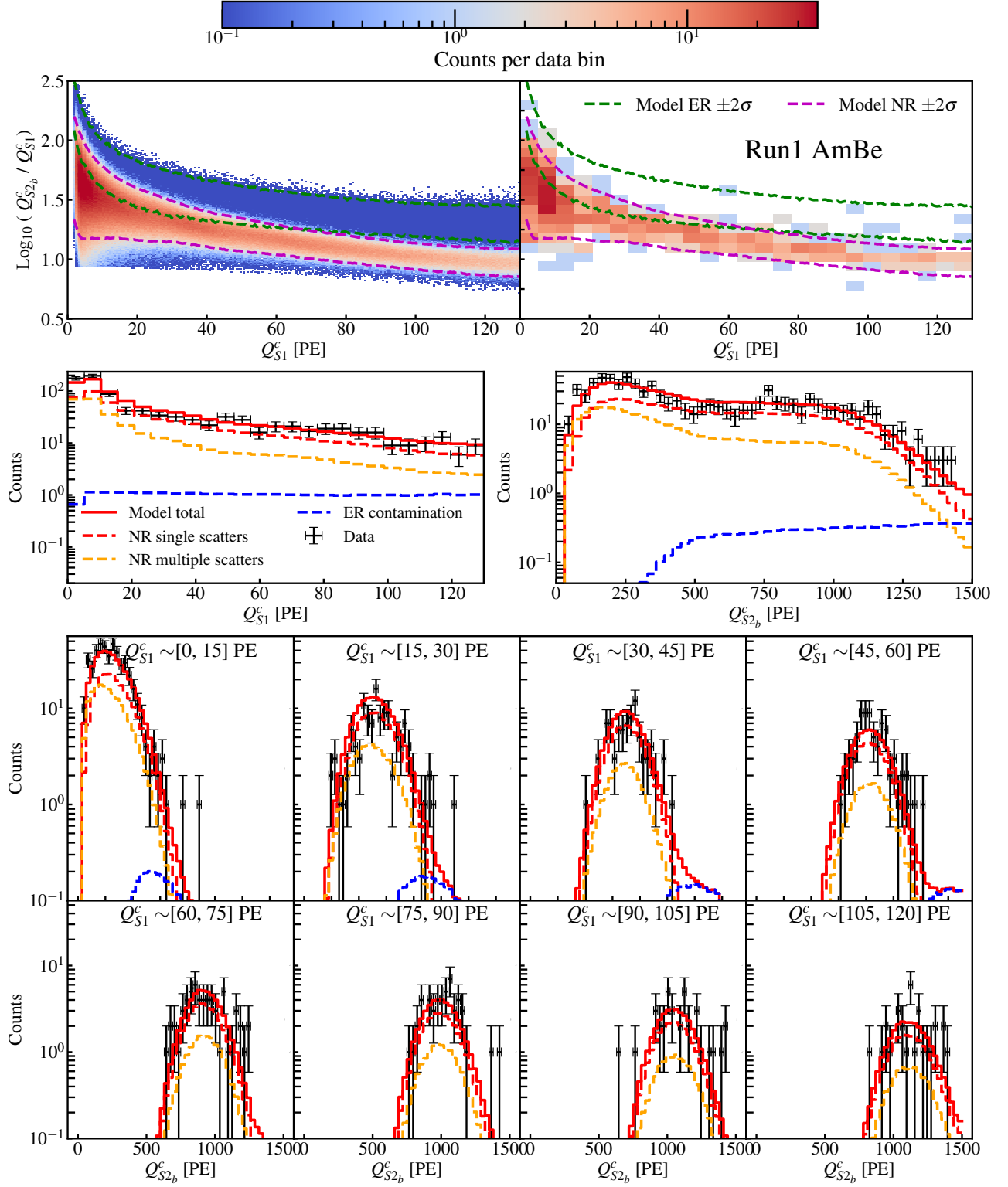


FIG. 22. The comparison between $^{241}\text{AmBe}$ neutron calibration data in Run1 and best-fit results of P4-NEST model from the simultaneous fit using Run0 and Run1 data. The figure layout and the line denotations are the same as Fig. 19.

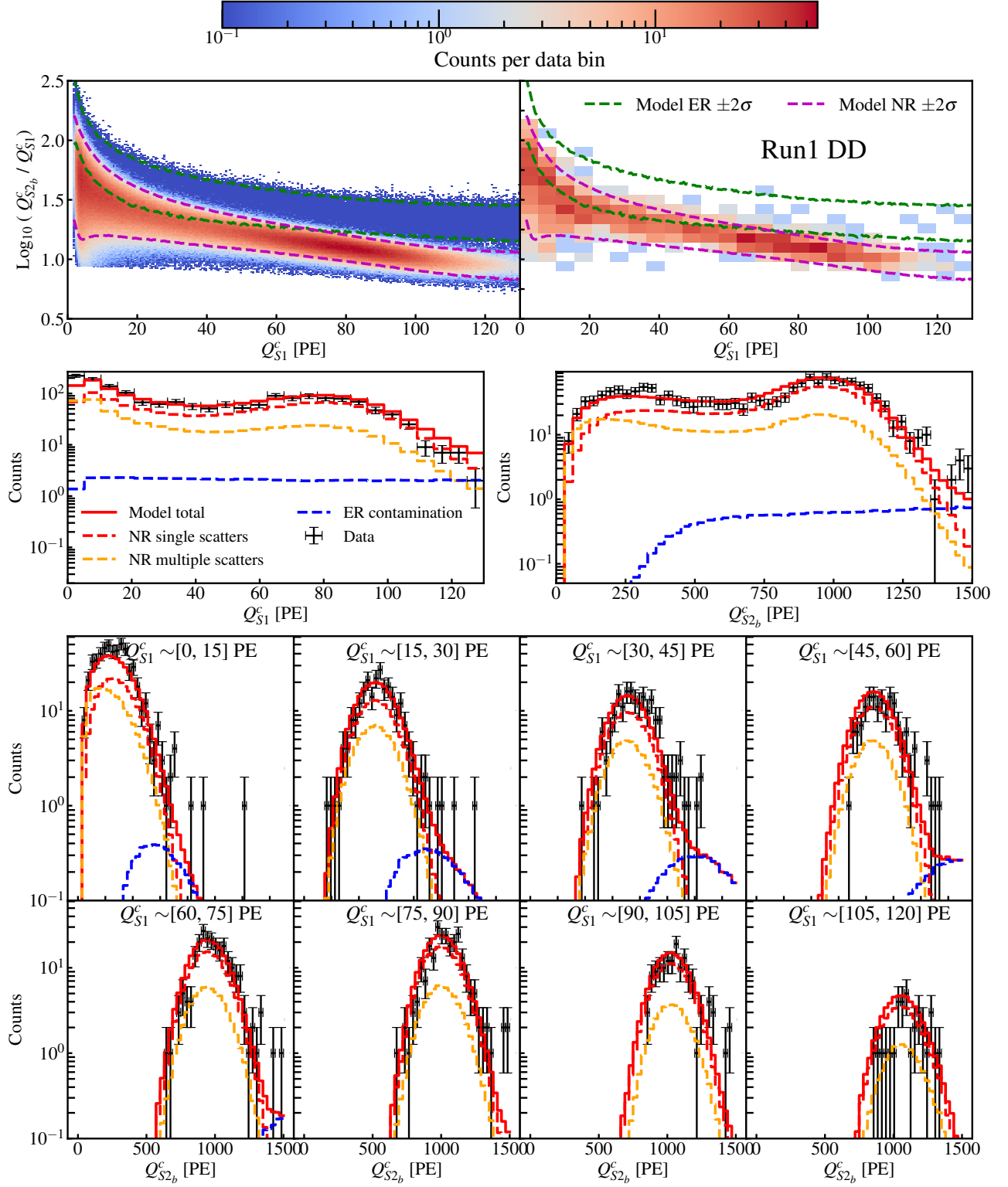


FIG. 23. The comparison between DD neutron calibration data in Run1 and best-fit results of P4-NEST model from the simultaneous fit using Run0 and Run1 data. The figure layout and the line denotations are the same as Fig. 19.

from those in Run0. This difference could be attributed to various factors, such as the disabling of some PMTs, differences in liquid level, and variations in the electric field configuration during Run1. The differences in the mean values of $Q_{S_1}^c$ and $Q_{S_{2b}}^c$ for the α events between Run0 and Run1 were utilized to constrain the ratio of g_1 and g_{2b} between the two runs.

$$\begin{cases} g_{1,\text{Run1}} &= f_{g_1} \cdot g_{1,\text{Run0}} \\ g_{2b,\text{Run1}} &= f_{g_{2b}} \cdot g_{2b,\text{Run0}} \end{cases} \quad (21)$$

The comparisons of the $Q_{S_1}^c$ distribution, the $Q_{S_{2b}}^c$ distribution, and the $Q_{S_{2b}}^c$ distributions at different $Q_{S_1}^c$ between the data and the best-fit model (all calibration data with Run0 and Run1 combined) are shown from Fig. 18 to 23.

VIII. SUMMARY

The article provides a comprehensive description of the signal response model employed in the PandaX-4T experiment. The model encompasses various processes, including the generation of intrinsic photons and electrons within the LXe, the detection and collection of photon and electron signals, as well as the subsequent signal reconstruction, correction, and selection processes. Considerable effort has been made to ensure a realistic representation of these processes within the signal response model. However, it is important to note that the production of photon and electron signals in LXe, particularly in the low-energy range, is subject to significant uncertainty, due to limited measurements in this range. To address this, the parameters of the signal response model have been refined through a simultaneous fit utilizing all available calibration data from both Run0 and Run1. Comparing the observed data with the signal response model, a good agreement has been achieved. Furthermore, future data taking in the PandaX-4T experiment is expected to yield additional information with an upgraded detector. This anticipated increase in data volume and improved detector capabilities will enable more stringent constraints on the signal response model, thereby reducing the associated uncertainty.

ACKNOWLEDGEMENTS

This project is supported in part by grants from National Science Foundation of China (Nos. 12090060, 12090061, 12205181), a grant from the Ministry of Science and Technology of China (No. 2023YFA1606200), and by Office of Science and Technology, Shanghai Municipal Government (grant No. 22JC1410100). We thank for the support from Double First Class Plan of the Shanghai Jiao Tong University. We also thank the sponsorship from the Chinese Academy of Sciences Center for Excellence

in Particle Physics (CCEPP), Hongwen Foundation in Hong Kong, Tencent Foundation in China, and Yangyang Development Fund. Finally, we thank the CJPL administration and the Yalong River Hydropower Development Company Ltd. for indispensable logistical support and other help.

Appendix A: Parameterization of recombination

The key parameters, which describe the recombination process in LXe, include the excited-atom-to-ion ratio (α), the Lindhard factor for nuclear recoils (L), the initial mean recombination fraction ($\langle r \rangle_0$), and the initial recombination fluctuation (Δr_0). The expressions for these parameters to ER and NR, respectively, are shown in Eq. A1 and A2, with ρ_{Xe} and E being the LXe density and field strength. Φ represents the error function.

Appendix B: Fit results with Run0 data only

A combined fit to all the calibration data (^{220}Rn , $^{241}\text{AmBe}$, and D-D calibration) in Run0 is performed. Table III summarizes the nominal values and best-fit values of both the free and constrained parameters obtained from the fits. The best-fit parameters are in good consistency with the nominals. The comparisons of the $Q_{S_1}^c$ distribution, the $Q_{S_{2b}}^c$ distribution, and the $Q_{S_{2b}}^c$ distributions at different $Q_{S_1}^c$ between the data and the best-fit model (all calibration data combined) are shown in Fig. 24, Fig. 25 and Fig. 26.

$$\begin{cases}
\alpha = (0.067366 + 0.093963\rho_{Xe}) \cdot \Phi(0.05\xi) \\
\langle r \rangle_0^{\text{ER}} = 1 - \frac{\langle N_e \rangle_{\text{ER}}}{\langle N_i \rangle_{\text{ER}}} \\
\Delta r_0^{\text{ER}} = A e^{-(\zeta_{\text{ER}} - 0.5)^2 / 0.084} (1 + \Phi(-0.6899(\zeta_{\text{ER}} - 0.5))) \\
\eta = 1 + \frac{0.4607}{(1 + (E/621.74)^{-2.2717})^{53.503}} \\
Y_0 = \frac{1000}{W} + 6.5 \left(1 - \frac{1}{1 + (E/47.408)^{1.9851}} \right) \\
Y_1 = 32.99\eta \left(1 - \frac{1}{1 + (E/(0.02672e^{\rho_{Xe}/0.3393}))^{0.6705}} \right), \\
\tau = \left(1652.264 + \frac{1.145935e10 - 1652.3}{1 + (E/0.02673)^{1.564691}} \right) \xi^{-2} \\
\langle N_e \rangle_{\text{ER}} = \xi \left(Y_1 + \frac{Y_0 - Y_1}{(1 + 1.304\xi^{2.1393})^{0.35535}} + \frac{28}{1 + \tau} \right) \\
\langle N_i \rangle_{\text{ER}} = 1000\xi/(W\alpha) \\
A = 0.1383 - 0.09583/(1 + (E/1210.)^{1.25}) \\
\zeta_{\text{ER}} = \langle N_e \rangle_{\text{ER}} W / (1000\xi)
\end{cases} \quad \text{for ER, where} \quad (\text{A1})$$

$$\begin{cases}
\alpha = \frac{(\langle N_e \rangle_{\text{NR}} + \langle N_{\text{ph}} \rangle_{\text{NR}})\zeta - 1}{\langle N_i \rangle_{\text{NR}}} \\
L = (\langle N_{\text{ph}} \rangle_{\text{NR}} + \langle N_e \rangle_{\text{NR}})W/\xi \\
\langle r \rangle_0^{\text{NR}} = 1 - \frac{\langle N_e \rangle_{\text{NR}}}{\langle N_i \rangle_{\text{NR}}} \\
\Delta r_0^{\text{NR}} = 0.1e^{-(\zeta_{\text{NR}} - 0.5)^2 / 0.0722} \\
\zeta = 0.0480E^{-0.0533}(\rho_{Xe}/2.90)^{0.30} \\
\langle N_e \rangle_{\text{NR}} = \xi \left(1 - \frac{1}{1 + (\xi/0.3)^2} \right) / (\zeta\sqrt{\xi + 12.6}) \\
\langle N_{\text{ph}} \rangle_{\text{NR}} = (11.0\xi^{1.1} - \langle N_e \rangle_{\text{NR}}) \left(1 - \frac{1}{1 + (\xi/0.3)^2} \right), \\
\langle N_i \rangle_{\text{NR}} = 4 \left(e^{\langle N_e \rangle_{\text{NR}}\zeta/4} - 1 \right) / \zeta \\
\zeta_{\text{NR}} = \langle N_e \rangle_{\text{NR}} W / (1000\xi)
\end{cases} \quad \text{for NR, with} \quad (\text{A2})$$

- [1] V. C. Rubin, W. K. Ford Jr, and N. Thonnard, *Astrophysical Journal*, Part 1, vol. 238, June 1, 1980, p. 471-487. **238**, 471 (1980).
- [2] D. Clowe, M. Bradač, A. H. Gonzalez, M. Markevitch, S. W. Randall, C. Jones, and D. Zaritsky, *The Astrophysical Journal* **648**, L109 (2006).
- [3] P. A. Ade, N. Aghanim, M. Arnaud, M. Ashdown, J. Aumont, C. Baccigalupi, A. Banday, R. Barreiro, J. Bartlett, N. Bartolo, et al., *Astronomy & Astrophysics* **594**, A13 (2016).
- [4] F. Zwicky, *Helvetica Physica Acta*, Vol. 6, p. 110-127 **6**, 110 (1933).
- [5] G. Bertone, D. Hooper, and J. Silk, *Physics reports* **405**, 279 (2005).
- [6] G. Jungman, M. Kamionkowski, and K. Griest, *Physics Reports* **267**, 195 (1996).
- [7] J. L. Feng, *Annual Review of Astronomy and Astrophysics* **48**, 495 (2010).
- [8] X. Xiao et al. (PandaX-I), *Phys. Rev. D* **92**, 052004 (2015).
- [9] A. Tan et al. (PandaX-II), *Phys. Rev. Lett.* **117**, 121303 (2016).
- [10] E. Aprile, J. Aalbers, F. Agostini, M. Alfonsi, L. Althueser, F. Amaro, M. Anthony, F. Arneodo, L. Baudis, et al., *Physical Review Letters* **121**, 111302 (2018).
- [11] D. Akerib et al. (LUX), *Phys. Rev. Lett.* **118**, 021303 (2017).
- [12] R. Agnese, T. Aramaki, I. Arnquist, W. Baker, D. Balakishiyeva, S. Banik, D. Barker, R. B. Thakur, D. Bauer, T. Binder, et al., *Physical Review Letters* **120**, 061802 (2018).
- [13] F. Petricca, G. Angloher, P. Bauer, A. Bento, C. Bucci, L. Canonica, X. Defay, A. Erb, F. v Feilitzsch, N. F. Iachellini, et al., in *Journal of Physics: Conference Series* (IOP Publishing, 2020), vol. 1342, p. 012076.
- [14] Y. Meng, Z. Wang, Y. Tao, A. Abdugerim, Z. Bo, W. Chen, X. Chen, Y. Chen, C. Cheng, Y. Cheng, et al., *Physical Review Letters* **127**, 261802 (2021).
- [15] E. Aprile, K. Abe, F. Agostini, S. A. Maouloud, L. Althueser, B. Andrieu, E. Angelino, J. Angevaere, V. Antochi, D. A. Martin, et al., *Physical Review Letters* **131**, 041003 (2023).
- [16] L.-Z. Collaboration et al., *Physical Review Letters* **131**, 041002 (2023).
- [17] W. Ma, A. Abdugerim, C. Cheng, Z. Bo, W. Chen, X. Chen, Y. Chen, Z. Cheng, X. Cui, Y. Fan, et al., *Physical Review Letters* **130**, 021802 (2023).
- [18] S. Li, M. Wu, A. Abdugerim, Z. Bo, W. Chen, X. Chen, Y. Chen, C. Cheng, Z. Cheng, X. Cui, et al., *Physical Review Letters* **130**, 261001 (2023).
- [19] L. Gu, A. Abdugerim, Z. Bo, W. Chen, X. Chen, Y. Chen, C. Cheng, Y. Cheng, Z. Cheng, X. Cui, et al., *Physical Review Letters* **129**, 161803 (2022).
- [20] D. Zhang, A. Abdugerim, Z. Bo, W. Chen, X. Chen, Y. Chen, C. Cheng, Z. Cheng, X. Cui, Y. Fan, et al., *Physical Review Letters* **129**, 161804 (2022).
- [21] M. Szydagis, N. Barry, K. Kazkaz, J. Mock, D. Stolp, M. Sweany, M. Tripathi, S. Uvarov, N. Walsh, and M. Woods, *Journal of Instrumentation* **6**, P10002 (2011).
- [22] M. Szydagis et al., *Noble Element Simulation Technique v2.0* (2018), URL <https://doi.org/10.5281/zenodo.1314669>.
- [23] X. Collaboration, E. Aprile, J. Aalbers, F. Agostini, M. Alfonsi, L. Althueser, F. Amaro, V. Antochi, F. Arneodo, L. Baudis, et al., *Physical Review D* **99**, 112009 (2019).
- [24] J. Lindhard, *Danske Videnskabernes Selskab, Matematisk-fysiske Meddelelser* **34**, 14 (1963).
- [25] A. Hitachi, T. Takahashi, N. Funayama, K. Masuda, J. Kikuchi, and T. Doke, *Physical Review B* **27**, 5279 (1983).
- [26] D. Akerib, S. Alsum, H. Araújo, X. Bai, A. Bailey, J. Balajthy, P. Beltrame, E. Bernard, A. Bernstein, T. Biesiadzinski, et al., *Physical Review D* **95**, 012008 (2017).
- [27] J. B. Birks, *Proceedings of the Physical Society. Section A* **64**, 874 (1951).
- [28] J. Thomas and D. A. Imel, *Physical Review A* **36**, 614 (1987).
- [29] C. Faham, V. Gehman, A. Currie, A. Dobi, P. Sorensen, and R. Gaitskell, *Journal of Instrumentation* **10**, P09010 (2015).
- [30] Note1, the number of peaks in a signal waveform refers to the count of times the signal exceeds 1/3 of its maximum amplitude and then falls below 1/10 of its maximum amplitude.
- [31] J. Li et al., arXiv preprint arXiv:2312.11072 (2023).
- [32] D. Zhang, A. Tan, A. Abdugerim, W. Chen, X. Chen, Y. Chen, C. Cheng, X. Cui, Y. Fan, D. Fang, et al., *Journal of Instrumentation* **16**, P11040 (2021).
- [33] S. Agostinelli and et al., *Nuclear Instruments and Methods in Physics Research Section A: Accelerators, Spectrometers, Detectors and Associated Equipment* **506**, 250 (2003).
- [34] M. Weber, Ph.D. thesis, Ruprecht-Karls-Universität Heidelberg (2013).
- [35] X. Chen, C. Cheng, M. Fu, F. Giuliani, J. Liu, X. Lu, X. Ji, Z. Qian, H. Qiao, Q. Wang, et al., *Journal of Instrumentation* **16**, T09004 (2021).
- [36] M. Szydagis, J. Balajthy, G. A. Block, J. P. Brodsky, E. Brown, J. E. Cutter, S. J. Farrell, J. Huang, E. S. Kozlova, C. S. Liebenthal, et al., *A review of nest models, and their application to improvement of particle identification in liquid xenon experiments* (2023), 2211.10726.
- [37] C. E. Dahl, Ph.D. thesis, Princeton University, New Jersey (2009).
- [38] D. Foreman-Mackey, D. W. Hogg, D. Lang, and J. Goodman, *Publications of the Astronomical Society of the Pacific* **125**, 306 (2013), 1202.3665.
- [39] J. Goodman and J. Weare, *Communications in Applied Mathematics and Computational Science* **5**, 65 (2010), 1002.2597.
- [40] Note2, the fit results using only Run0 data can be found in Appendix B.
- [41] A. Gelman, J. B. Carlin, H. S. Stern, D. B. Dunson, A. Vehtari, and D. B. Rubin, *Statistical Science* **7**, 457 (1992).

Parameters	Description	Constrain	Nominal	Best-fit	Note & reference
p_{dpe}	Double-PE probability	fixed	0.22	-	(Eq. 4)
τ_e	Electron lifetime	fixed*	-	-	Time dependent (Eq. 5, Fig. 1)
ϵ_{ext}	Electron extraction efficiency	fixed*	-	-	Correlated with g_2 and κ (Eq. 6)
κ	Electron amplification factor	fixed*	-	-	Time dependent (Eq. 7 & Fig. 2)
g_1	$S1$ gain	free	-	$0.0998^{+0.0011}_{-0.0009}$	Extra constraint on reconstructed energy (Eq. 8 & Sec. VIII D)
-	$S2$ gain	free	-	$3.95^{+0.12}_{-0.14}$	$S1$ dependent (Eq. 9 & Fig. 6)
ϵ_{hit}	Loss probability of 1 hit due to clustering	fixed*	-	-	$S1$ dependent (Eq. 10 & Fig. 6)
δ_{S1}^{self}	self-trigger bias on $S1$	fixed*	-	-	$S2$ dependent (Eq. 11 & Fig. 6)
$\Delta\delta_{S1}^{self}$	Standard deviation of self-trigger bias	fixed*	-	-	$S2$ dependent (Eq. 13 & Fig. 5)
δ_{S2}	Mean $S2$ reconstruction bias	fixed*	-	-	Depend on various variables (Eq. 16 & Fig. 15)
$\Delta\delta_{S2}$	Standard deviation of reconstruction bias	fixed*	-	-	Depend on various variables (Eq. 16 & Fig. 15)
σ_{pos}	Position reconstruction resolution	fixed*	-	-	Special implementation in fast MC (Sec. VI)
ϵ_q	Quality cut efficiency	fixed*	-	-	
ϵ_r	ROI efficiency	fixed*	-	-	
ϵ_{rec}	Signal reconstruction efficiency	fixed*	-	-	
ϵ_{ss}	Single scatter cut efficiency	fixed*	-	-	
p_{ER}^{ER}				$1.0^{+0.7}_{-0.15}$	
p_{ER}^{ER}				$-2.8^{+1.5}_{-1.5}$	
p_{ER}^{ER}				$2.0^{+1.5}_{-0.9}$	
p_2				$-1.5^{+0.8}_{-1.2}$	
p_3				$0.4^{+0.4}_{-0.5}$	
p_0				-0.7 ± -1.1	(Eq. 17 & Sec. VIIC)
p_1				0.6 ± 0.8	
p_2				$-0.2^{+0.5}_{-0.6}$	
p_3				1.16 ± 0.07	
A^{ER}				$1.09^{+0.12}_{-0.09}$	
A^{NR}				$0.027^{+0.008}_{-0.009}$	
R_{ER}^{AmBe}				0.027 ± 0.013	(Sec. VIII E)
R_{ER}^{DD}				$0.015^{+0.005}_{-0.004}$	
$R_{T,Run0}^{Rn}$	Ratio of Tritium's contamination in Run0 Rn	constrained	0.010 ± 0.006	-	
R_{AmBe}^{AmBe}	Ratio of AC contamination to NR in AmBe	fixed	0.0038	-	
R_{AC}^{DD}	Ratio of AC contamination to NR in DD	fixed	0.0021	-	
	3rd-order Legendre coefficients for ER				
	3rd-order Legendre coefficients for NR	free			
	Recombination fluctuation scaling for ER				
	Recombination fluctuation scaling for NR				
	Ratio of ER contamination to NR in AmBe				
	Ratio of ER contamination to NR in DD				
	Ratio of Tritium's contamination in Run0 Rn				
	Ratio of AC contamination to NR in AmBe				
	Ratio of AC contamination to NR in DD				

TABLE III. Parameters of the Run0-only fit.

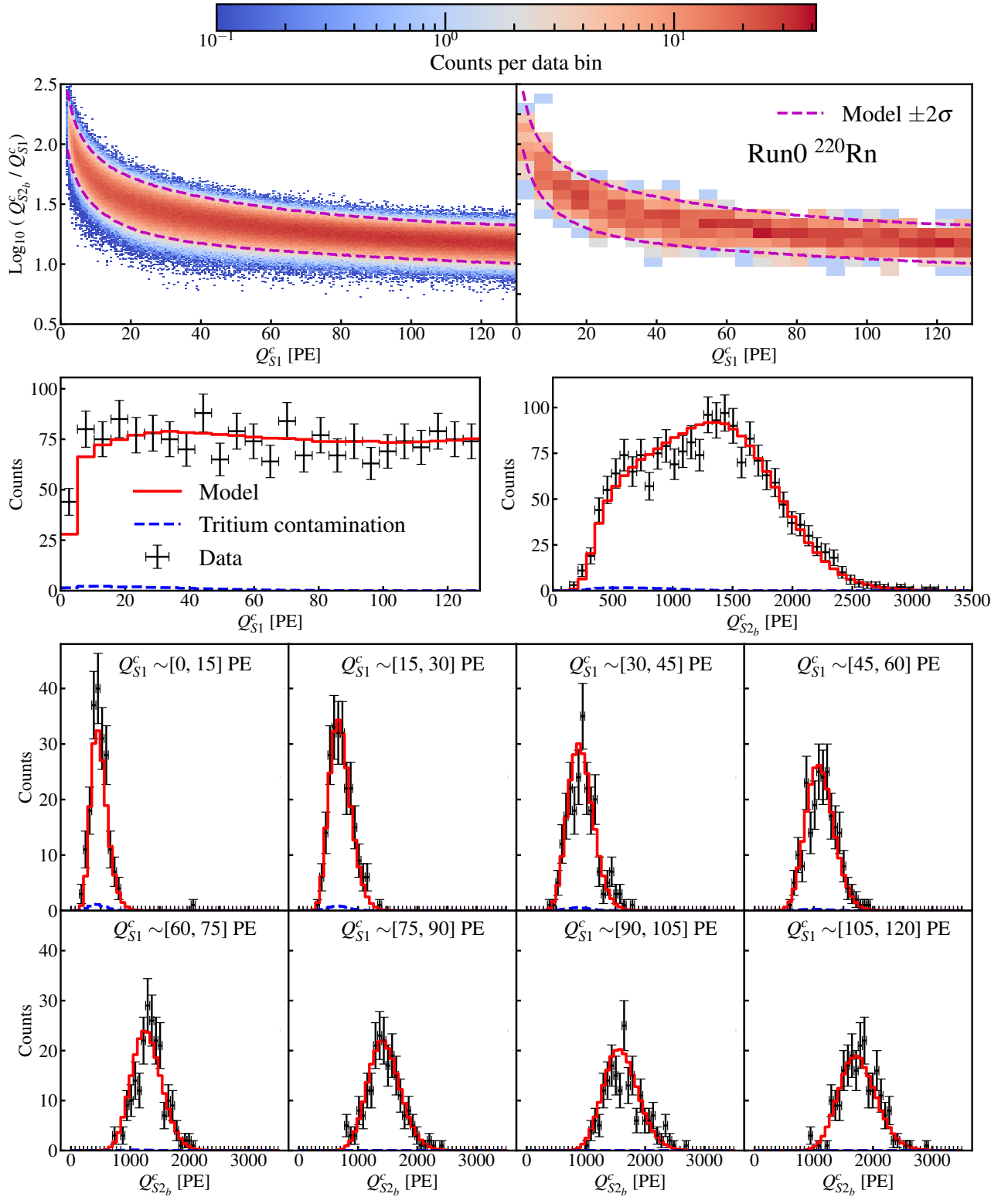


FIG. 24. The comparison between ^{220}Rn calibration data in Run0 and best-fit results of P4-NEST model. The figure layout and the line denotations are the same as Fig. 18.

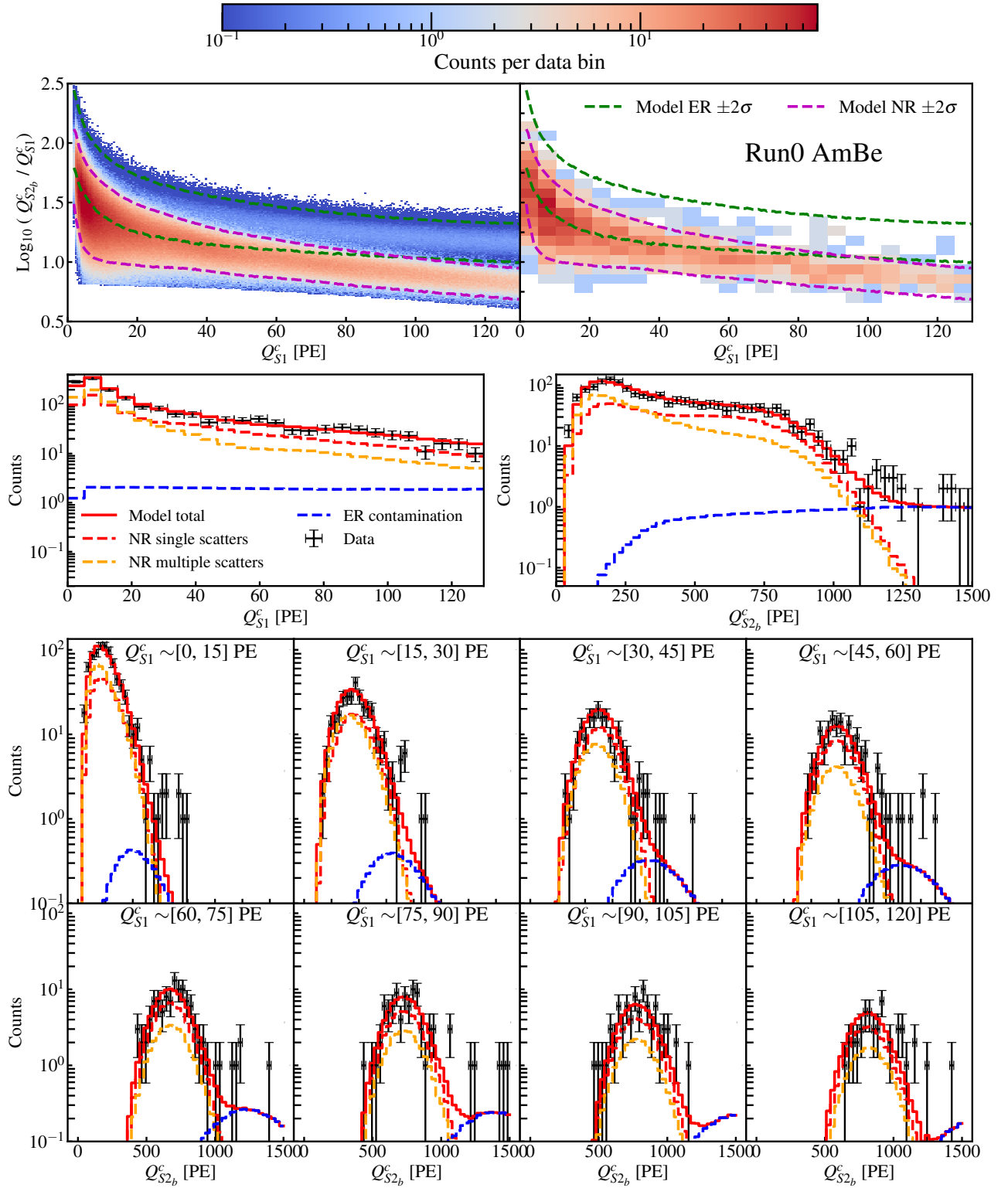


FIG. 25. The comparison between $^{241}\text{AmBe}$ calibration data in Run0 and best-fit results of P4-NEST model. The figure layout and the line denotations are the same as Fig. 19.

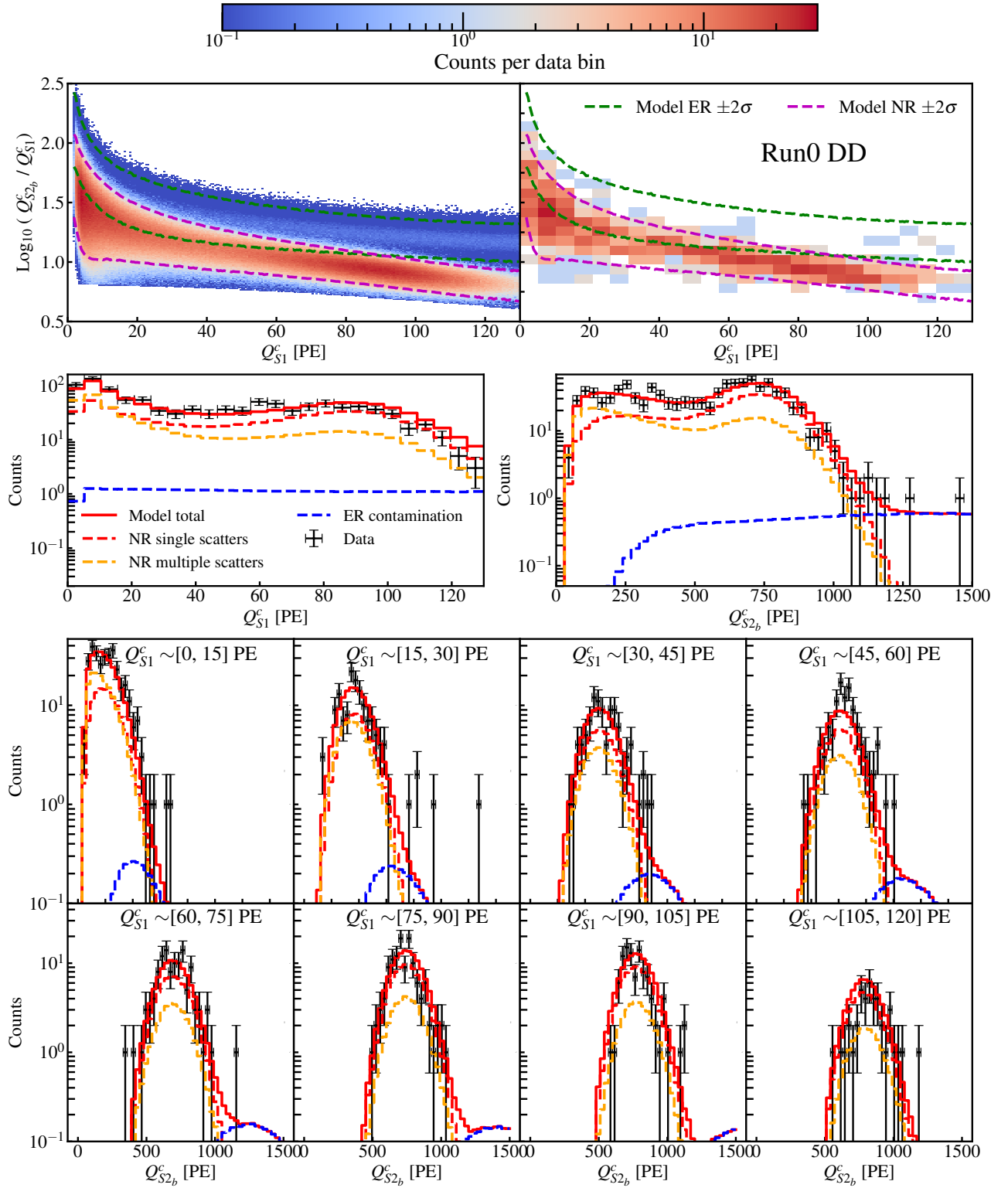


FIG. 26. The comparison between DD neutron calibration data in Run0 and best-fit results of P4-NEST model. The figure layout and the line denotations are the same as Fig. 19.